

Radial Basis Function Techniques for Neural Field Models on Surfaces

Sage B. Shaw^{*1}, Zachary P. Kilpatrick^{†1}, and Daniele Avitabile^{‡2,3}

¹Department of Applied Mathematics, University of Colorado Boulder, Boulder, CO 80309 USA

²Department of Mathematics, Vrije Universiteit Amsterdam, The Netherlands

³Inria MathNeuro team, Montpellier, France

Abstract

We present a numerical framework for solving neural field equations on surfaces using Radial Basis Function (RBF) interpolation and quadrature. Neural field models describe the evolution of macroscopic brain activity, but modeling studies often overlook the complex geometry of curved cortical domains. Traditional numerical methods, such as finite element or spectral methods, can be computationally expensive and challenging to implement on irregular domains. In contrast, RBF-based methods provide a flexible alternative by offering interpolation and quadrature schemes that efficiently handle arbitrary geometries with high-order accuracy. We first develop an RBF-based interpolatory projection framework for neural field models on general surfaces. Quadrature for both flat and curved domains are derived in detail, ensuring high-order accuracy and stability as they depend on RBF hyperparameters (basis functions, augmenting polynomials, and stencil size). Through numerical experiments, we demonstrate the convergence of our method, highlighting its advantages over traditional approaches in terms of flexibility and accuracy. We conclude with an exposition of numerical simulations of spatiotemporal activity on complex surfaces, illustrating the method's ability to capture complex wave propagation patterns.

1 Introduction

Neural field equations are nonlinear integro-differential equations used as large-scale models of neuronal activity, providing tractable equations amenable to analysis and simulations on a diversity of domains [1, 10, 64]. Large-scale neuronal activity is strongly determined by the architecture of synaptic connections between neurons [17]. Associated models typically grapple with the high volume of neurons and synapses, especially in primate cortex, with approximations such as coarsening, homogenization, and timescale separations [8, 28]. Neural fields describe cortical domains as continuum excitable media and their network connectivity as a weight kernel within a nonlinear integral operator, allowing us to apply theory from nonlinear waves and other methods from partial differential equations (PDE) [10]. This kernel defines a spatially dependent coupling function that assigns synaptic strength based on the locations of pre- and post-synaptic neurons. Most analyses and simulations of neural fields therefore focus on the treatment and effects of this nonlinear and nonlocal interaction term as it conveys local dynamics throughout the domain.

The derivation of neural fields is grounded in the known spatial and functional structure of synaptic connectivity throughout cerebral cortex, justifying the typical spatial coarse graining required to attain the standard model [57, 65]. For the convenience of analysis and simulation, most modeling studies consider spatial domains and connectivity functions that take canonical forms (e.g., distance-dependent weight kernels on planar domains) [18]. This has yielded considerable dividends in the understanding of the wide diversity of spatiotemporal dynamics these models can support, as well as novel theory for the stability of solutions to nonlocal equations. In seminal work, Amari (1977) simplified the nonlinearity appearing on the integral as a Heaviside step function [1], allowing for the implementation of interface methods and direct construction of traveling wave solutions [20, 44]. Cleverly chosen weight kernels with rational Fourier transforms allow for the conversion of nonlocal neural fields to local PDE for more efficient analysis and simulation [21, 37]. However, tractable models often

*Sage.Shaw@colorado.edu

†zpkilpat@colorado.edu

‡d.avitabile@vu.nl

overlook more complex geometries. Here we advance a method that is highly flexible to the formulation of neural fields on arbitrary domains with curvature and nonstandard weight kernels.

Realistic observable cortical domains are often two dimensional surfaces with curvature embedded in three dimensional space. While the cortex itself is of course three-dimensional, imaging studies most commonly access neural activity on the surface via functional magnetic resonance or voltage sensitive dye imaging [31, 38]. Modeling efforts in this direction have focused on prototypical curved domains such as the sphere [12, 52, 62] or the torus [35]. Solutions on such domains can then be conveniently expressed using spectral methods with clean and complete orthogonal eigenbases, but complex domains, that are not expressed as Cartesian products, cannot leverage this approach. Recently, there has been interest in simulating neural fields on arbitrary smooth surfaces [41], but so far the associated algorithms have no theoretical convergence guarantees, and empirical error measurements suggest the method is only accurate to first order.

A framework for assessing convergence for any projection-based numerical neural-field solver was recently developed in [4]. This approach decomposes numerical error in the solution into three main components: the error made by the spatial projection, the error from numerical time-integration, and the error from the quadrature. Importantly, the paper provides a unified operator-theoretic formulation that enables rigorous convergence analysis for Galerkin and collocation schemes. This analysis not only clarifies how the error scales with spatial resolution, but also guides the development of more efficient discretizations for neural field simulations on complex geometries.

In the current work, we present a high-order numerical method for neural field simulations, and partially address theory regarding numerical convergence within the projection method framework. This high-order accuracy is achieved using radial basis function formulae for quadrature (RBF-QF) [49–51] and radial basis function (RBF) interpolation as the projector. High-order methods are essential to allow for simulations of neural field equations onto complex surfaces, as they allow for high accuracy for fewer computational resources. Specifically, approximating the integral operator using a quadrature on a mesh with n points, requires $O(n^2)$ operations¹. In Section 2 we describe the mathematical framework for collocation and projection schemes for neural field models, formulate the associated discrete ODEs, and state convergence results for projection schemes. In Section 3 we review the RBF-QF algorithm first for flat domains, then for smooth closed manifolds, highlighting the role of local interpolation and the construction of projection-based quadrature on curved geometries. In Section 4 we conduct several numerical experiments verifying convergence rates for RBF-QF and our new neural field solver. In Section 5 we demonstrate the power of this method by simulating several interesting neural field systems on non-trivial domains.

2 Collocation schemes for the neural field model

We consider, as a model problem, a neural field posed on a compact domain $(t, \mathbf{x}) \in [0, T] \times (D \subset \mathbb{R}^{\dim})$:

$$\begin{aligned} \partial_t u(t, \mathbf{x}) &= -u(t, \mathbf{x}) + g(t, \mathbf{x}) + \int_D w(\mathbf{x}, \mathbf{y}) f(u(\mathbf{y}, t)) d\mu(\mathbf{y}), \\ u(0, \mathbf{x}) &= v(\mathbf{x}). \end{aligned} \tag{1}$$

We assume the integral is on a volume or surface D , and so is expressed in terms of a measure μ . Heuristically, a collocation scheme for eq. (1) can be conceived in two steps, as follows:

Step 1: collocation. Select n points $\Xi = \{\mathbf{x}_i : i \in \mathbb{N}_n\} \subset D$ in the domain, where n may depend on a discretization parameter h so $n(h) \rightarrow \infty$ as $h \rightarrow 0$. We impose that eq. (1) holds at each node, that is, we *collocate the equation* on Ξ . This leads to a functional equation relating $\{\partial_t u(t, \mathbf{x}_i)\}_i$ and $\{u(t, \mathbf{x}_i)\}_i$ to the function $u(t, _)$, appearing under the integral of eq. (1).

Step 2: quadrature. Select a quadrature for the integral, in terms of $\{u(t, \mathbf{x}_i)\}_i$ and obtain a system of coupled, nonlinear ordinary differential equations (ODEs).

Avitabile (2023) [4] builds on previous work by Atkinson (2005) [3] to show that convergence estimates for collocation (and other) schemes are still possible when disregarding **Step 2**. **Step 1** is a fully functional scheme for which one can estimate convergence rates of the collocation (or other projection types) as $n \rightarrow \infty$. **Step 2** further approximates the projection with quadrature, establishing a new scheme (a *discrete collocation scheme* in Atkinson’s terminology [3]).

¹For certain domains, one can leverage the FFT to achieve $O(n \log n)$ complexity, but these methods do not generalize to arbitrary surfaces.

2.1 Interpolatory projection

RBFs provide a flexible and accurate way to interpolate functions and have been successfully applied to nonlinear PDEs with complex spatiotemporal dynamics, like reaction–diffusion systems [54]. Since our goal is to approximate nonlinear integrodifferential (neural field) equations, RBF-based collocation schemes are a natural choice. We present these schemes using the abstract notion of an *interpolating projector*, which maps functions onto their interpolants (e.g., RBFs).

In this setup, one seeks a solution u to the neural field equations as a mapping on $[0, T]$ to $\mathbb{X} = C(D)$, the space of continuous functions on D . An interpolatory projector P_n linearly projects any function $v \in \mathbb{X}$ to a function $v_n = P_n v$ in an n -dimensional subspace $\mathbb{X}_n = \text{Span}\{L_1, \dots, L_n\} \subset \mathbb{X}$, with the property

$$P_n: \mathbb{X} \rightarrow \mathbb{X}_n, \quad P_n v = v, \quad \text{on } \Xi. \quad (2)$$

The approximant then takes the form

$$v_n(\mathbf{x}) := (P_n v)(\mathbf{x}) = \sum_{j=1}^n v(\mathbf{x}_j) L_j(\mathbf{x}), \quad \mathbf{x} \in D,$$

and a useful characterization of interpolatory projectors is the following (See [2, 3] and [4, adapted from Proposition 4.1]):

Proposition 2.1 (Characterization of interpolatory projectors). *If a projection operator $P_n: \mathbb{X} \rightarrow \mathbb{X}_n$ satisfies the interpolation condition eq. (2), then for any $r \in \mathbb{X}$*

$$P_n r = 0 \quad \text{on } D \quad \text{if and only if,} \quad P_n r = 0 \quad \text{on } \Xi. \quad (3)$$

This property is useful when the function r is a residual error, as we will see in a moment.

2.2 General hypotheses

In order to formulate the neural field problem in operator form, we make the following standing assumptions.

Hypothesis 2.1 (General hypotheses). *1. The cortical domain $D \subset \mathbb{R}^{\dim}$ is compact.*

2. The temporal domain $J \equiv [0, T] \subset \mathbb{R}$ is compact.

3. The synaptic kernel $w: D \times D \rightarrow \mathbb{R}$ is a function in $C(D \times D)$.

4. The firing rate $f: \mathbb{R} \rightarrow \mathbb{R}$ is a bounded and everywhere differentiable Lipschitz function, which guarantees $f, f' \in B(\mathbb{R})$.

5. The initial condition $v: D \rightarrow \mathbb{R}$ is a function in $\mathbb{X} = C(D)$.

6. The forcing $g: D \times J \rightarrow \mathbb{R}$ is a function in $C(J, \mathbb{X})$.

As shown in [4], Hypothesis 2.1 provides a natural functional setup for the neural field problem posed on $\mathbb{X} = C(D)$, minimally extending [48] to compact cortices D and for studying numerical schemes. It is possible to deal with more generic kernels than the one considered here, but we restrict our work to continuous kernels for simplicity of exposition. Frameworks in [4, 48] could be leveraged for such extensions.

2.3 Neural field in operator form

To set the stage for our collocation scheme, we first rewrite the neural field eq. (1) in operator form

$$\begin{aligned} u'(t) &= -u(t) + WF(u(t)) + g(t) =: N(t, u(t)), \quad t \in J \equiv [0, T], \\ u(0) &= v, \end{aligned} \quad (4)$$

where we define the integral operator W and nonlinear operator F :

$$W: \mathbb{X} \rightarrow \mathbb{X}, \quad v \mapsto \int_D w(_, \mathbf{y}) v(\mathbf{y}) d\mu(\mathbf{y}), \quad F: \mathbb{X} \rightarrow \mathbb{X}, \quad v \mapsto f(v). \quad (5)$$

Note, eq. (1) evolves the \mathbb{R} -valued function $u: D \times J \rightarrow \mathbb{R}$, whereas eq. (4) evolves the \mathbb{X} -valued function $U: J \rightarrow \mathbb{X}$, $t \mapsto u(_, t)$. With a small abuse of notation, we adopt the same symbol for both functions (u), as for the forcing function g .

eq. (4) describes a Cauchy problem on the Banach space \mathbb{X} , which is well-posed under Hypothesis 2.1. That is, there exists a unique $u \in C^1(J, \mathbb{X})$ satisfying eq. (4), as shown in [4, Lemma 2.7] (See [48] for analogous results on unbounded cortices).

2.4 Step 1: collocation scheme

The collocation scheme approximates the solution u of eq. (4), by a function $u_n \in C^1(J, \mathbb{X}_n)$, that satisfies the following Cauchy problem on the n -dimensional subspace $\mathbb{X}_n \subset \mathbb{X}$:

$$\begin{aligned} u_n'(t) &= -u_n(t) + P_n W F(u_n(t)) + P_n g(t) = P_n N(t, u_n(t)), & t \in J, \\ u_n(0) &= P_n v, \end{aligned} \quad (6)$$

that is, the Cauchy problem obtained from eq. (4) upon applying the projection P_n to the vectorfield N , and to the initial condition v .

In view of proposition 2.1, this is equivalent to imposing that eq. (1) holds at all $\mathbf{x}_i \in \Xi$ (hence we have collocated the equation, and completed **Step 1**). That is, we require the eq. (1) to hold exactly at the collocation points $\{\mathbf{x}_i\}_{i=1}^n$, reducing the infinite-dimensional problem to a finite-dimensional system of ODEs. In [4, Theorem 3.1] it is shown that, under Hypothesis 2.1, also the projected problem is well-posed, admitting a unique solution $u_n \in C^1(J, \mathbb{X}_n)$.

The projected eq. (6) evolves the function $u_n(t)$ in \mathbb{X}_n . This form is useful in the analysis of the scheme, but for implementations we pursue an ODE approximating the n coefficients $\alpha_i(t) := u_n(t)(\mathbf{x}_i)$ using eq. (3), which lets us pass from eq. (6) to an equivalent ODE in \mathbb{R}^n . We define the residual

$$R: C^1(J, \mathbb{X}) \rightarrow C(J, \mathbb{X}), \quad u \mapsto u' - N(_, u),$$

and rewrite eq. (6) as

$$P_n(R(u_n)(t)) = 0, \quad t \in J, \quad P_n(u_n(0) - v) = 0,$$

which, by property eq. (3) is equivalent to

$$\begin{aligned} u_n'(t)(\mathbf{x}_i) &= [P_n N(t, u_n(t))](\mathbf{x}_i), & (i, t) \in \mathbb{N}_n \times J, \\ u_n(0)(\mathbf{x}_i) &= (P_n v)(\mathbf{x}_i). \end{aligned}$$

Since $u_n(t) \in \mathbb{X}_n$, we set $u_n(t) = \sum_{j \in \mathbb{N}_n} \alpha_j(t) L_j$, exploit the Lagrange property of the basis $\{L_j\}$, and obtain an ODE in \mathbb{R}^n

$$\begin{aligned} \alpha'(t) &= -\alpha(t) + K(\alpha(t)) + \gamma(t) & t \in J, \\ \alpha(0) &= v \end{aligned} \quad (7)$$

where

$$\begin{aligned} \alpha_i(t) &= u_n(t)(\mathbf{x}_i), \quad v_i = v(\mathbf{x}_i), \\ \gamma_i(t) &= g(\mathbf{x}_i, t), \quad K_i(\alpha) = \int_D w(\mathbf{x}_i, \mathbf{y}) f\left(\sum_{j \in \mathbb{N}_n} \alpha_j L_j(\mathbf{y})\right) d\mu(\mathbf{y}). \end{aligned}$$

We stress that eq. (6) and eq. (7) are equivalent Cauchy problems on the n -dimensional phase spaces \mathbb{X}_n and \mathbb{R}^n , respectively.

2.5 Step 2: quadrature and Discrete Projection Schemes

The ODE eq. (7) on \mathbb{R}^n is not yet implementable on a computer, because generally the integrals in K can not be evaluated in closed form, and must be approximated by numerical quadrature. Such an approach generates a computationally implementable algorithm using *Discrete Projection Schemes*.

We use a quadrature scheme induced by interpolation. We will later discuss the details of the quadrature, which approximates the integral operator

$$Q: \mathbb{X} \rightarrow \mathbb{R}, \quad Qv = \int_D v(\mathbf{y}) d\mu(\mathbf{y})$$

with a sum of the form

$$Q_n: \mathbb{X} \rightarrow \mathbb{R}, \quad Q_n v = \sum_{j=1}^n v(\mathbf{x}_j) \mu_j.$$

We can apply the quadrature scheme Q_n to the operator W in eq. (6), define

$$W_n: \mathbb{X} \rightarrow \mathbb{X}_n, \quad (W_n v)(\mathbf{x}) = Q_n(w(\mathbf{x}, _)v), \quad (8)$$

and arrive at the scheme

$$\begin{aligned} \tilde{u}'_n(t) &= -\tilde{u}_n(t) + P_n W_n F(\tilde{u}_n(t)) + P_n g(t), \quad t \in J, \\ \tilde{u}_n(0) &= P_n v, \end{aligned} \quad (9)$$

the ODE system for u at the collocated points, approximated by quadrature.

Following similar steps to Section 2.4, we use proposition 2.1 to obtain

$$\begin{aligned} \tilde{\alpha}'(t) &= -\tilde{\alpha}(t) + \tilde{K}(\tilde{\alpha}(t)) + \gamma(t) \quad t \in J, \\ \alpha(0) &= v, \end{aligned} \quad (10)$$

for the evolution of the vector of coefficients $\alpha(t) = [\alpha_1(t), \dots, \alpha_n(t)]^T$, where

$$\begin{aligned} \tilde{\alpha}_i(t) &= \tilde{u}_n(t)(\mathbf{x}_i), \quad v_i = v(\mathbf{x}_i), \\ \gamma_i(t) &= g(t, \mathbf{x}_i), \quad \tilde{K}_i(\tilde{\alpha}) = \sum_{j=1}^n w(\mathbf{x}_i, \mathbf{x}_j) f\left(\sum_{k \in \mathbb{N}_n} \tilde{\alpha}_k L_k(\mathbf{x}_j)\right) \mu_j. \end{aligned}$$

2.6 Convergence of the collocation scheme

In [4], Atkinson's approach for studying projection methods in Fredholm and Hammerstein integral equations [2, 3], is extended to time-dependent neural field equations. The central result of the paper is a bound for the error $\|u - u_n\|_{C(J, \mathbb{X})}$ in terms of the projection error $\|u - P_n u\|_{C(J, \mathbb{X})}$, that is, a bound for the collocation scheme in **Step 1**, in terms of the error of the interpolating projector.

Theorem 2.1 (Abridged from [4], Theorem 3.3 and discussion on page 570). *Under Hypothesis 2.1, if $P_n v \rightarrow v$ for all $v \in \mathbb{X}$, then $u_n \rightarrow u$ in $C(J, \mathbb{X})$. Further, there exist positive constants m and M , independent of n , such that*

$$m\|u - P_n u\|_{C(J, \mathbb{X})} \leq \|u - u_n\|_{C(J, \mathbb{X})} \leq M\|u - P_n u\|_{C(J, \mathbb{X})}.$$

Since the time interval J is compact it holds $\|u - P_n u\|_{C(J, \mathbb{X})} = \|u(t_*) - P_n u(t_*)\|_{\mathbb{X}}$ for some $t_* \in J$, and thus the convergence rate of the collocation scheme is estimated from the interpolation error $\|v - P_n v\|_{\mathbb{X}}$ for some $v \in \mathbb{X}$.

The error of the Discrete Collocation Scheme can in principle be estimated, given $\|u - \tilde{u}_n\| \leq \|u - u_n\| + \|u_n - \tilde{u}_n\|$, but we do not take this route here. Controlling $\|u_n - \tilde{u}_n\|$ requires rigorous error estimates for quadrature rules on curved domains D which, to the best of our knowledge, are not yet available when the underlying interpolant is an RBF. Instead, we proceed in the remaining sections as follows:

1. We employ RBF interpolants whose interpolation error $\|P_n v - v\|$ is available in literature, and deduce rates for the error of collocation scheme $\|u - u_n\|$, as per theorem 2.1.
2. We select a quadrature scheme built on RBFs, for which we provide numerical evidence of convergence rates. A guiding principle is to select a quadrature rule that matches the error of the collocation scheme.
3. We provide numerical evidence of convergence rates for the error $\|u - \tilde{u}_n\|$ of the fully discrete scheme in cases where an analytical solution to the neural field is available in closed form.

3 RBF interpolation and quadrature

We use RBFs for the interpolatory projector P_n and quadrature formula Q_n introduced in Section 2. In particular, we use RBF quadrature formulae (RBF-QF), which provide an interpolation-based technique to calculate quadrature weights for arbitrary sets of quadrature nodes with high-order accuracy. This quadrature is geometrically flexible: it works in domains of arbitrary dimension and in complex geometry. The approximation power comes from the remarkable properties of radial basis function (RBF) interpolation. In this section, we describe the algorithm used to interpolate functions, generate quadrature weights in flat and curved domains, and discuss the consequences of hyperparameter choices. This general approach can then be leveraged to implement our neural field approximation scheme.

3.1 Local Interpolation

The first use of RBF interpolation was by Hardy in 1971 [30] to construct a topography from scattered elevation measurements. The interpolant was a linear combination of radially-symmetric basis functions called *Multiquadrics*. Critically, the centers of these basis functions coincided with the locations of the measurements, and as a result, the interpolants were guaranteed to exist and be unique. The Mairhuber-Curtis theorem shows that such guarantees break down when basis functions are chosen independently of the interpolation nodes [22, 23, 40] as occurs in multivariate polynomial interpolation. Later developments showed that other radially symmetric basis functions could be used similarly, with resulting interpolants exhibiting spectral convergence as the number of nodes increased [14, 67]. For a comprehensive introduction to RBF interpolation, see Fasshauer (2007) [23].

The price of spectral convergence, however, is that finding interpolant coefficients requires solving an $n \times n$ linear system, which becomes prohibitively expensive and ill-conditioned as n (the number of interpolation nodes) increases. There are two approaches to remedy this limitation. First, one can choose compactly supported basis functions, often called Wendland functions [23, 63], to produce a sparse, banded linear systems, which can be solved efficiently. We opt for the second approach: local RBF interpolation using polyharmonic splines and appended polynomial basis functions, which is the focus of this subsection.

Given a compact domain $D \subset \mathbb{R}^{\dim}$, we seek an approximation to a sufficiently smooth function $f : D \rightarrow \mathbb{R}$, using a discrete finite set of interpolation nodes $\Xi_n \subset D$, and a partition of the domain $\{E_j\}_{j=1}^m$. We will approximate f piecewise on each element E_j , where each piecewise component will be a linear combination of basis functions. For each element E_j , there is an associated subset of interpolation nodes $S(E_j) \subseteq \Xi_n$, which we call a stencil. Generally, the elements E_j are small polygons that shrink or are divided as more points are added. The stencil $S(E_j)$ contains the closest k points in Ξ_n to a suitably-defined center of E_j , making $k = |S(E_j)|$ a hyper-parameter called the *stencil size*. In what follows, we will sometimes use E to refer to a generic element in the partition $\{E_j\}_{j=1}^m$.

Partitions are demonstrated in two examples depicted in Figure 3.1. The Delaunay triangulation is popular for partitioning planar domains and widely integrated into many standard mathematical software libraries [26]. Interpolation nodes are used as the vertices of triangular elements that form the partition (Figure 3.1A). The defining feature of the Delaunay triangulation is that a circle circumscribing each triangular element contains no other interpolation nodes except its vertices. Alternatively, Voronoi partitions (Figure 3.1B) assign each element a single interpolation node and define it as the set of points in D closer to that node than to any other. The Voronoi diagram is the geometric dual of the Delaunay triangulation for a given set of points².

We will refer to $\{E_j\}_{j=1}^m$ as the partition, mesh, or triangulation interchangeably and the subsets E_j as elements (of the partition), patches, or triangles depending on the context. While our presentation allows for general choices of interpolation nodes and meshes, not all such combinations yield accurate or stable interpolants. A useful quantity associated with the nodes is the *covering radius* [15, 23]

$$h = \sup_{x \in D} \min_{y \in \Xi_n} \|x - y\|, \quad (11)$$

the supremum of the radii of circles with centers $x \in D$ that contain no interpolation nodes. The covering radius is analogous to mesh spacing and scales asymptotically as $h \sim n^{-1/\dim}$, as in regular grids.

This notion arises naturally both the Delaunay triangulation and Voronoi partition. In the Delaunay case, the radius of any element's circumscribed circle (See Figure 3.1A) provides a lower bound on h , and if the triangulation covers D , then h is the maximum of these radii across all triangular elements. In the Voronoi case, the covering radius is the maximum distance from a node to a vertex of its associated patch. Figure 3.1B shows a circle centered on a Voronoi vertex with radius equal to the distance to the adjacent nodes. In both cases, the covering radius is the maximum over a finite set of such radii, making it computationally straightforward.

Going forward, we assume each stencil has fixed size $|S(E)| = k$ for all $E \in \{E_j\}_{j=1}^m$. We introduce a parameter, “deg”, to control the order of accuracy of our interpolant. Over each element E , the approximation is expressed as a linear combination of RBFs φ_y and polynomial basis functions $\pi_\alpha(x) = x^\alpha$, where α is a multi-index, and $\{\pi_\alpha\}_{|\alpha| \leq \text{deg}}$ forms a basis for $\mathbb{P}_{\text{deg}}(D)$, the space polynomials of degree at most deg. A function $f \in C(D)$ is then approximated using the piecewise-defined

²This is almost always true. Non-uniqueness can arise when a Voronoi vertex is shared by more than three cells (e.g., in a Cartesian grid), but this is rare for randomly chosen points and can be resolved by small perturbations.

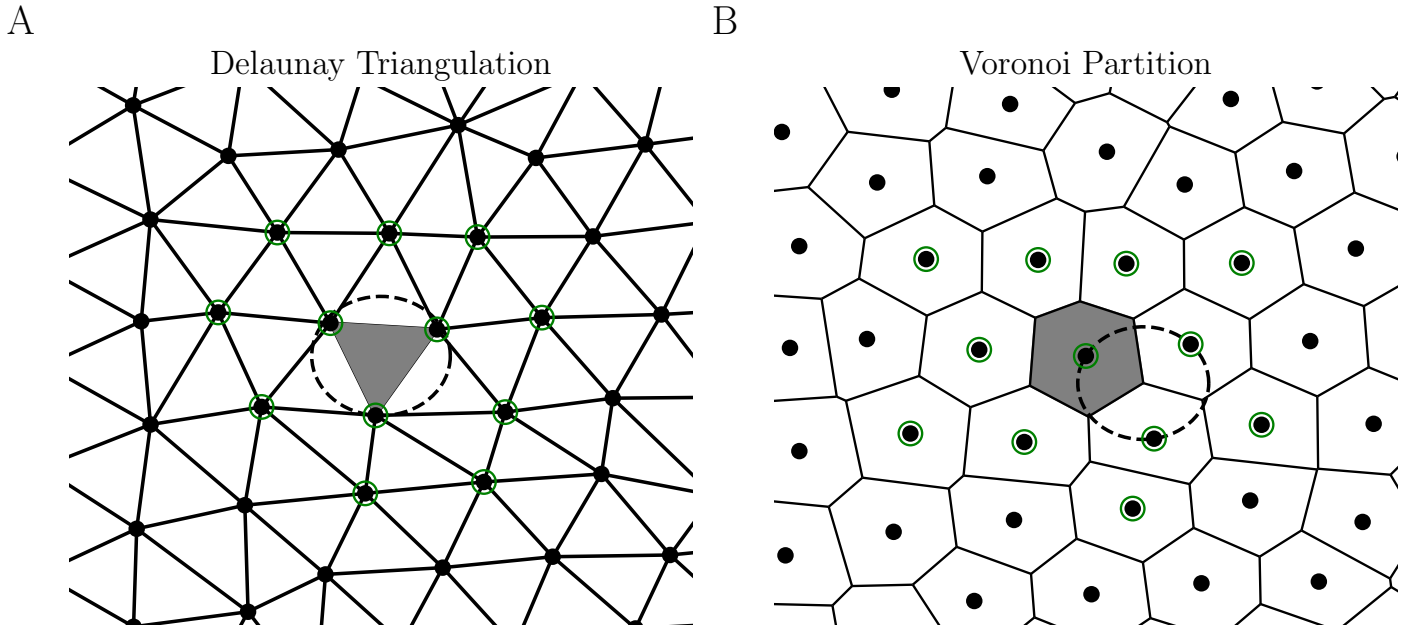


Figure 3.1: **Stencils.** Each panel shows a subset of the interpolation nodes Ξ_n (black dots), the boundaries (solid lines) enclosing partition elements E_j , and an example element (shaded gray) and its stencil points (green circles). **A.** Delaunay triangulations partition elements using interpolation nodes as vertices. An element’s circumscribing circle does not contain any additional interpolation nodes. **B.** Voronoi partitions assign one interpolation node per element. A circle centered at a Voronoi vertex can always be drawn to contain only the centers of neighboring elements.

function

$$s(\mathbf{x}) := \sum_{j=1}^m s_{E_j}(\mathbf{x}) \chi_{E_j}(\mathbf{x}), \quad \mathbf{x} \in D, \quad (12)$$

where $\chi_E: D \rightarrow \mathbb{R}$ is the indicator function on E and where s_E is the function

$$s_E(\mathbf{x}) = \sum_{\mathbf{y} \in S(E)} c_{E,\mathbf{y}} \varphi_{\mathbf{y}}(\mathbf{x}) + \sum_{|\alpha| \leq \text{deg}} d_{E,\alpha} \pi_{\alpha}(\mathbf{x}).$$

The RBFs $\psi_{\mathbf{y}}$ are each translates of the same *basic function* $\psi_{\mathbf{y}}(\mathbf{x}) = \Phi(\|\mathbf{x} - \mathbf{y}\|)$ [23], but not all radially symmetric functions are suitable basic functions. We will restrict ourselves to polyharmonic splines

$$\Phi(r) = \begin{cases} r^{\ell}, & \text{for } \ell \text{ odd,} \\ r^{\ell} \log(r), & \text{for } \ell \text{ even.} \end{cases} \quad (13)$$

To determine the coefficients $c_{\mathbf{y}}$ and d_{α} we enforce two sets of conditions known as *interpolation conditions* and *moment conditions*, respectively:

$$\begin{aligned} f(\mathbf{x}) &= s_E(\mathbf{x}), & \text{for } \mathbf{x} \in S(E), & \quad (\text{interpolation}) \\ 0 &= \sum_{\mathbf{y} \in S(E)} d_{\alpha} \mathbf{y}^{\alpha}, & \text{for } |\alpha| \leq \text{deg.} & \quad (\text{moment}) \end{aligned}$$

Note that though we refer to these as “interpolation conditions”, a point $\mathbf{x} \in S(E)$ but $\mathbf{x} \notin E$ contributes to the interpolant s_E , but not necessarily the global piecewise interpolant s . The full approximation interpolates f at each $\mathbf{x} \in \Xi$ since every node lies in some element E , but each local interpolant s_E satisfies additional conditions not directly reflected in the global approximation.

The moment conditions ensure *polynomial reproduction*: for any $p \in \mathbb{P}_{\text{deg}}(D)$, the local interpolant satisfies $s_E = p$ on its domain. This property underpins the approximation power of the local interpolation scheme.

Thus, the coefficients are determined by solving the linear system

$$\begin{bmatrix} A & \Pi \\ \Pi^T & 0 \end{bmatrix} \begin{bmatrix} \mathbf{c} \\ \mathbf{d} \end{bmatrix} = \begin{bmatrix} \mathbf{f}_E \\ \mathbf{0} \end{bmatrix} \quad (14)$$

where the full block matrix is the *interpolation matrix*. Here, $A_{ij} = \Phi(\|\mathbf{x}_i - \mathbf{x}_j\|)$ is the *RBF interpolation matrix*, $\Pi_{i,\alpha} = \mathbf{x}_i^\alpha$ is the *polynomial matrix*, and $(\mathbf{f}_E)_i = f(\mathbf{x}_i)$ for $\mathbf{x}_i \in S(E)$.

Before turning to error estimation and convergence theory, we comment on key parameters in the RBF interpolant. We recommend first choosing deg , the degree of the appended polynomial, which governs the order of accuracy as $h \rightarrow 0$. This choice determines the size of the polynomial matrix Π , which must have more rows than columns to ensure the system eq. (14) is invertible. Specifically, the stencil size must satisfy $k \geq \binom{\text{deg} + \text{dim}}{\text{deg}}$.

We will specify our choice of k for all numerical experiments, though there are often reasons to choose k larger than the minimum. As general principle, increasing deg improves accuracy, while increasing k enhances stability. For instance, near domain boundaries, stencils may become one-sided, potentially reducing accuracy due to Runge's phenomenon. Enlarging stencils in such regions can mitigate this effect and improve accuracy without changing h . For further discussion on the interplay between stencil size and polynomial degree, see [6, 7, 24].

We must also choose ℓ , the degree of the polyharmonic spline (see eq. (13)). While increasing ℓ can reduce approximation error [24], the improvement diminishes quickly. More importantly, polyharmonic splines are *conditionally positive definite*, and the interpolation matrix eq. (14) is guaranteed to be non-singular if $\text{deg} \leq \lfloor \ell/2 \rfloor + 1$ [23, 63].

We conclude this section by interpreting the interpolant s defined in eq. (12) as a projection $P_n f$, aligning this step with the framework in Section 2. While the projection operator $P_n : C(D) \rightarrow C(D)$ is expected to preserve continuity, the interpolant s is constructed locally and may be discontinuous across element boundaries. A continuous projector P_n can be obtained by applying weighted averages to neighboring local interpolants.

For example, consider a Voronoi partition $\{V_i\}_{i=1}^n$ of D , and let $\{T_{i,j,k}\}$ denote the associated Delaunay triangulation, where $1 \leq i, j, k \leq n$ index the vertices of the triangle. For any $\mathbf{x} \in T_{i,j,k} \subseteq D$, let $b_{i,\mathbf{x}}, b_{j,\mathbf{x}}, b_{k,\mathbf{x}}$ be the barycentric coordinates of \mathbf{x} with respect to $\mathbf{x}_i, \mathbf{x}_j, \mathbf{x}_k \in \Xi$. We define the piecewise projector

$$(P_n f)(\mathbf{x}) = \sum_{T_{i,j,k}} \chi_{T_{i,j,k}}(\mathbf{x}) \left(b_{i,\mathbf{x}} s_{V_i}(\mathbf{x}) + b_{j,\mathbf{x}} s_{V_j}(\mathbf{x}) + b_{k,\mathbf{x}} s_{V_k}(\mathbf{x}) \right),$$

which is continuous across D and smooth within each triangle. With P_n defined, the Lagrange basis $\{L_1, \dots, L_n\}$ is given by $L_i = P_n v_i$ where each $v_i \in C(D)$ satisfies $v_i(\mathbf{x}_j) = \delta_{ij}$.

Second, the projection method requires $P_n f \rightarrow f$ as $n \rightarrow \infty$ but the relationship between n and our interpolant is not apparent. To relate them, we consider a sequence of interpolation node sets $\{\Xi_n\}$ with covering radii $h(\Xi_n) \rightarrow 0$ as in eq. (11). Such sequences can be easily constructed by refining triangulations or by placing points to efficiently fill the domain.

This framing aligns with interpolation convergence theorems in the literature which establish error bounds for polyharmonic spline interpolation such as

$$\|f - P_n f\|_\infty \leq C h^{\text{deg}}$$

or better in some cases [15, 23, 32, 63]. These results apply to *global* interpolation ($k = n$). While we found no published proof that *local* interpolation achieves the same rate, we expect such a result could follow from adaptations of the existing global proofs [23, 63], though it would likely require geometric justification that the cone condition can be relaxed, except near boundaries. In practice, studies using local interpolation offer numerical evidence of convergence, often showing convergence rates faster than $O(h^{\text{deg}})$ [6, 7, 24] which we observe in Section 4.

3.2 Quadrature In Flat Domains

The theory of RBF-QF has its roots in finite difference methods, known as RBF-FD. Both quadrature and differentiation are linear functionals – linear maps into \mathbb{R} – and share a common theoretical foundation. Derivative approximation using RBFs was introduced first [33], and the modern RBF-FD method based on local interpolation was discovered independently by several groups shortly after [16, 58, 59, 66]. Due to this history, some authors refer to RBF-QF as a variant of RBF-FD, though it produces quadrature rather than finite difference weights. We begin with the general theory for approximating

linear functionals, then specialize to quadrature. This approach clarifies the distinction between RBF-QF and RBF-FD, and highlights when and why a mesh is needed.

To approximate a linear functional \mathcal{L} (such as quadrature or differentiation at a point) applied to a function $f : D \rightarrow \mathbb{R}$, we first consider the local RBF interpolant $s : D \rightarrow \mathbb{R}$ which, by eq. (12), gives

$$\mathcal{L}f \approx \mathcal{L}s = \sum_E \mathcal{L}S_E \chi_E = \sum_E \sum_{\mathbf{y} \in S(E)} c_{E,\mathbf{y}} \mathcal{L}(\varphi_{\mathbf{y}} \chi_E) + \sum_{|\alpha| \leq \text{deg}} d_{E,\alpha} \mathcal{L}[\chi_E \pi_\alpha].$$

The coefficients $c_{E,\mathbf{y}}$ and $d_{E,\alpha}$ are given in vector form in eq. (14). Representing the previous equation as a sum over dot products, we have

$$\begin{aligned} \mathcal{L}f &\approx \sum_E [\mathcal{L}\varphi \quad \mathcal{L}\pi] \begin{bmatrix} \mathbf{c} \\ \mathbf{d} \end{bmatrix} = \sum_E [\mathcal{L}\varphi \quad \mathcal{L}\pi] \begin{bmatrix} A & \Pi \\ \Pi^T & 0 \end{bmatrix}^{-1} \begin{bmatrix} \mathbf{f} \\ \mathbf{0} \end{bmatrix}, \\ &= \sum_E [\mathbf{w}_E \quad \gamma_E] \begin{bmatrix} \mathbf{f}_E \\ \mathbf{0} \end{bmatrix} = \sum_{\mathbf{x}_i \in \Xi} w_{\mathbf{x}_i} f(\mathbf{x}_i), \\ &= \mathbf{w}^T \mathbf{f}, \end{aligned}$$

where \mathbf{w}_E denotes the element-wise functional weights, and \mathbf{w} the combined functional weights,

$$\mathbf{w}_E = \begin{bmatrix} A & \Pi \\ \Pi^T & 0 \end{bmatrix}^{-1} \begin{bmatrix} \mathcal{L}\varphi \\ \mathcal{L}\pi \end{bmatrix}, \quad (\mathbf{w})_{\mathbf{x}_i} = w_{\mathbf{x}_i} = \sum_{E: \mathbf{x}_i \in S(E)} (\mathbf{w}_E)_{\mathbf{x}_i}. \quad (15)$$

If \mathcal{L} is a differential (integral) operator, then \mathbf{w} represents finite difference (quadrature) weights. Moreover, the expressions involving $w_{\mathbf{x}_i}$ and \mathbf{w} help outline the implementation of the algorithm.

First, for each element E , we identify the stencil $S(E)$, and evaluate the functionals $\mathcal{L}(\varphi_{\mathbf{x}_i} \chi_E)$ and $\mathcal{L}(x^\alpha \chi_E)$. We then form the system in eq. (15) and solve for the weights \mathbf{w}_E , whose order reflects the ordering of the nodes in the stencil $S(E)$. Each node \mathbf{x}_i may appear in multiple stencils and thus be assigned several weights $(\mathbf{w}_E)_{\mathbf{x}_i}$. The final quadrature weights are obtained by summing all contributions associated with each node across stencils.

Since we focus on quadrature, we set $\mathcal{L}f = Qf = \int_D f(y) d\mu(y)$ as in Section 2. While our theory suggests $Q_n = QP_n$, we use the simpler form $Q_n = Qs = \mathbf{w}^T \mathbf{f}$, which offers the same accuracy as is easier to compute. Each functional evaluation $\mathcal{L}\varphi$, $\mathcal{L}\pi$ thus involves analytically integrating an RBF or polynomial basis function over an element E . The resulting quadrature approximation is then $Q_n f = \mathbf{w}^T \mathbf{f}$.

3.3 Quadrature on Smooth Closed Manifolds

When the cortical domain D is a 2-manifold with curvature, applying RBF-QF is more involved. Convergence theory for such schemes remains an active area of research [29], while implementations have been developed by Reeger and Fornberg [49–51]. We summarize their approach for smooth closed surfaces and refer to [51] for the treatment of surface boundaries. Numerical evidence of convergence rates is presented in Section 4.4.

The method begins with a set of interpolation nodes Ξ and defines two sets of elements. The first is a planar triangulation $\mathcal{E} = \cup_{j=1}^m E_j$ with nodes exactly equal to Ξ . The method is designed for curved (non-planar) domains where the cortical surface D does not coincide with \mathcal{E} . It constructs a second set of elements forming a partition $D = \cup_{j=1}^m \mathcal{T}_j$, where each \mathcal{T}_j is a curved triangular patch on D , in contrast to the flat triangles E_j in \mathcal{E} (See fig. 3.2). The two families share the interpolation nodes, $\Xi \subseteq D \cap \mathcal{E}$, and are paired such that for each j there exists a bijection $\mu_j(E_j) = \mathcal{T}_j$. We defer a precise definition of the mappings to a later section, and simply note that once the families $\{E_j\}$, $\{\mathcal{T}_j\}$, and $\{\mu_j\}$ are in place, one can write, without approximation,

$$\int_D f(\mathbf{x}) dS = \sum_{j=1}^m \int_{\mathcal{T}_j} f(\mathbf{x}) dS = \sum_{j=1}^m \int_{E_j} f(\mu_j(\boldsymbol{\xi})) \|(\partial_{\xi_1} \mu_j \times \partial_{\xi_2} \mu_j)(\boldsymbol{\xi})\| d\boldsymbol{\xi}, \quad (16)$$

in which $\|(\partial_{\xi_1} \mu_j \times \partial_{\xi_2} \mu_j)(\boldsymbol{\xi})\|$ is the Jacobian of μ_j at $\boldsymbol{\xi}$. The method introduced by Reeger and Fornberg amounts to [49–51]: (i) defining the mappings $\{\mu_j\}$; (ii) selecting a quadrature scheme for the integral over E_i , on the right-hand side of eq. (16).

The mappings $\{\mu_j\}$ depend on a set of *projection points* $\{\mathbf{p}_j\}$, as shown in Figure 3.2. For now, we assume these points are given and explain later how to determine them. For each fixed j , let π_j denote the plane in which the triangle E_j . We define

$$\mu_j: \pi_j \rightarrow D, \quad \boldsymbol{\xi} \mapsto \mathbf{x}$$

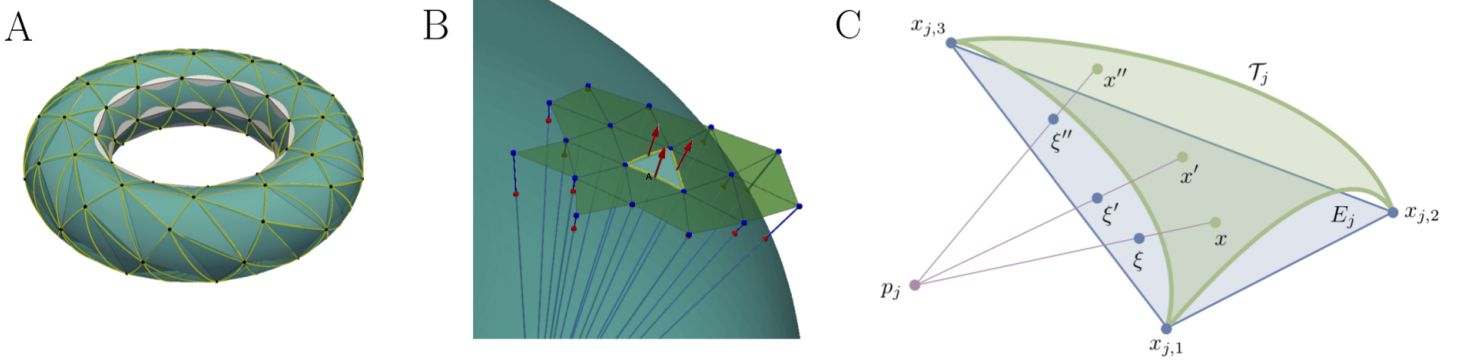


Figure 3.2: **A.** The surface of a torus (D_T , transparent light-green) is sampled at some well-distributed points (Ξ , black) which are then used for a triangulation ($\{E_j\}_{j=1}^M$, white flat triangles). Using the method described in Section 3.3, these planar triangles are projected onto the torus to form a partition of surface triangles ($\{\mathcal{T}_j\}_{j=1}^M$, outlined in yellow). **B.** Stencil and projected stencil of a flat triangle (E_j , white, but appears light green because it is behind the surface) from a surface triangulation. Nearby surface points form the stencil ($S(E_j)$, red) and are projected along lines (blue) emanating from the projection point, onto co-planar points (ξ , blue). The projection point is computed from the vertices of the triangle and approximated edge normals (red arrows). **C.** A detailed diagram relating a flat triangle E_j and its associated surface triangle \mathcal{T}_j . Points $x \in \pi_j$ on the plane of E_j are projected onto $\xi \in \pi_j$ along the lines through the projection point p_j .

where $x \in D$ is the closest point to $\xi \in \pi_j$ along the line connecting p_j and ξ . Such a point exists provided ξ lies in a sufficiently small neighborhood of E_j and the node set is Ξ is dense enough. The mapping μ_j then sends E_j to a curved triangle $\mathcal{T}_j \subseteq D$. This construction explains why $\{p_j\}$ are called projection points: if p_j were a light source, then \mathcal{T}_j would be the shadow of E_j cast onto the curved surface D . The point $x \in \mathcal{T}_j$ is defined as the closest such intersection since the projection line may intersect D more than once. Finally, we note that μ_j is defined for points on π_j even outside E_j .

By construction, E_j and \mathcal{T}_j intersect at the nodes $\{x_{j,1}, x_{j,2}, x_{j,3}\} \subset \Xi$ (See fig. 3.2). The mapping μ_j sends each edge of the planar triangle E_j connecting $x_{j,k}$ and $x_{j,l}$ to the corresponding edge of the curved patch \mathcal{T}_j , preserving endpoints. Each such edge, together with the projection point p_j , lies in a common *cutting plane*; thus p_j is the intersection of three cutting planes.

The definition of the mappings $\{\mu_j\}$ and the properties above are valid for any choice of projection points $\{p_j\}$. However, these points must be selected carefully to ensure that $\{\mathcal{T}_j\}$ forms a valid partition of D . Reeger and Fornberg outline a method to choose projection points based on the normal vectors $\{n_j\}$ of the planar triangles $\{E_j\}$. For any pair of adjacent triangles E_j and $E_{j'}$, sharing an edge $E_j \cap E_{j'}$, a necessary condition for $\{\mathcal{T}_j\}$ to partition D is that the maps μ_j and $\mu_{j'}$ both send the shared edge to the same curved edge in their respective curved triangles, that is

$$\mu_j(E_j \cap E_{j'}) = \mathcal{T}_j \cap \mathcal{T}_{j'} = \mu_{j'}(E_j \cap E_{j'}), \quad \text{for all } j \text{ and } j',$$

which implies that p_i and p_j must lie in the same cutting plane. They resolve this by choosing the cutting plane orthogonal to $n_j - n_{j'}$ with the condition $p_j \cdot (n_j - n_{j'}) = 0$. This approach determines the distribution $\{p_j\}$, as each planar triangle is associated with three such cutting planes, uniquely fixing its projection point.

Once the bijections $\{\mu_j\}$ are defined, a quadrature rule for integrands $g: E_j \rightarrow \mathbb{R}$ can be written as

$$\int_{E_j} g(\xi) d\xi \approx \sum_{r=1}^{q_j} g(\xi_{j,r}) \rho_{j,r},$$

where the quadrature nodes satisfy

$$\mu_j(\xi_{j,r}) = x_{j,r}, \quad r \in \mathbb{N}_{q_j}, \quad j \in \mathbb{N}_m,$$

and $\{x_{j,1}, \dots, x_{j,q_j}\} = S(E_j)$; that is, the quadrature nodes for E_j are the pre-images of the stencil points under μ_j (see Section 3.1 for a definition of $S(E_j)$). Importantly, the nodes $\{\xi_{j,r}\}_{r=1}^{q_j}$ lie in the plane π_j , but not necessarily within the triangle E_j itself, as illustrated in Figure 3.2. The points $\mu_j^{-1}(S(E_j)) \in \pi_j$ now form a planar stencil for E_j , and we use the procedure outlined in Section 3.2. Specifically, we treat each E_j as a flat domain and apply RBF-QF locally, using the basis functions evaluated at the stencil nodes and integrating them over E_j . This yields weights that, when paired with function evaluations on the surface at $x_{j,r} = \mu_j(\xi_{j,r})$, define a quadrature rule that approximates integrals over the curved domain D .

4 Numerical Experiments for Neural Fields

This section presents numerical experiments using RBF-QF, both as a standalone quadrature method and within a method of lines neural field simulation. We begin by introducing notation we will use throughout the section.

We consider three spatial domains of integration: (i) $D_1 = [0, 1]^2$, the unit square; (ii) $D_{2\pi} = [-\pi, \pi]^2$ the square of width 2π centered at the origin (iii) D_T , a torus with major radius $R = 3$ and minor radius of $r = 1$, parameterized by angles $(\varphi, \theta) \in D_{2\pi}$ as

$$\mathbf{x}(\varphi, \theta) = \begin{bmatrix} x(\varphi, \theta) \\ y(\varphi, \theta) \\ z(\varphi, \theta) \end{bmatrix} = \begin{bmatrix} (R + r \cos \theta) \cos \varphi \\ (R + r \cos \theta) \sin \varphi \\ r \sin \theta \end{bmatrix}. \quad (17)$$

We denote the inverse map by $\psi : D_T \rightarrow D_{2\pi}$.

Unless otherwise noted, we use the standard Euclidean distance metric in \mathbb{R}^2 or \mathbb{R}^3 , as appropriate, for stencil selection and evaluating basic function inputs. For certain test functions and neural field solutions on D_1 or $D_{2\pi}$, we instead use a doubly periodic distance metric with periods $\Lambda = 1$ and $\Lambda = 2\pi$, respectively, defined by

$$\text{dist}(\mathbf{x}, \mathbf{y}) = \min_{i,j=-1,0,1} \left\| \mathbf{x} - \mathbf{y} + \Lambda \left(i \begin{bmatrix} 1 \\ 0 \end{bmatrix} + j \begin{bmatrix} 0 \\ 1 \end{bmatrix} \right) \right\|. \quad (18)$$

Most of our test functions, as well as both neural field solutions, use scaled Gaussian functions defined with respect to this periodic distance:

$$\text{Gauss}(\mathbf{x}, \mathbf{y}; \sigma) = \frac{1}{2\pi\sigma^2} \exp \left[-\frac{1}{2\sigma^2} \text{dist}^2(\mathbf{x}, \mathbf{y}) \right]. \quad (19)$$

In this setting, the kernel function is defined as $w(\mathbf{x}, \mathbf{y}) = \tilde{w}(\text{dist}(\mathbf{x}, \mathbf{y}))$, where \tilde{w} is a standard radial function (e.g., Gaussian). While \tilde{w} is not periodic, periodicity is enforced via the modified distance function in eq. (18), which wraps Euclidean distance across boundaries—effectively defining w on a flat torus. This approach ensures that w depends on the shortest periodic path between \mathbf{x} and \mathbf{y} , not just their Euclidean separation.

In neural field simulations we use the sigmoidal firing rate function

$$f[u] = \left(1 + \exp(-\gamma(u - \vartheta)) \right)^{-1} \quad (20)$$

with gain $\gamma = 5$ and threshold $\vartheta = 1/2$.

To test the quadrature within a method of lines neural field simulation, we proceed with a *method of manufactured solutions* to construct equations with known analytic solutions. Specifically, we choose a solution $u(t, \mathbf{x})$ and define a forced neural field equation parameterized by a weight kernel w and the firing firing-rate function f :

$$\partial_t u(t, \mathbf{x}) = -u(t, \mathbf{x}) + \int_D w(\mathbf{x}, \mathbf{y}) f[u(\mathbf{y})] dy + F(t, \mathbf{x}) \quad (21)$$

where the forcing term F is chosen to ensure that u satisfies the equation exactly.

4.1 Node selection

We briefly describe our selection of quadrature nodes and triangular meshes in each domain. Rather than detailing each construction, we provide simplified description and refer interested readers to the Code availability section (section 6) for implementation details, including quadrature weight generation, node placement, and time integration. For the square domains D_1 and $D_{2\pi}$ we compare two node families. The first places interior nodes at the vertices of a regular equilateral triangle tiling, with equally spaced nodes along the boundary. We refer to this as the *regular grid*, since interior stencils are rotated translates of each other and yield identical weights (Figure 4.1E). The second family distributes random interior nodes using a deterministic point-repulsion process, again placing equally spaced nodes along the boundary. An example is shown in Figure 4.1C. In both cases, we use Delaunay triangulation of the quadrature nodes to define the mesh.

For quadrature nodes on the torus D_T , we use a deterministic regular grid of *spiral nodes*. They are defined by a triangular tiling of the parameter space $D_{2\pi}$ that avoids thin triangles when mapped onto the torus. The nodes lie on lines of constant θ (rotation around the minor axis) and are equally spaced in the φ -direction, but staggered so they form approximately 60° angles with the θ -constant lines. These angled lines in trace closed spiral paths on the torus surface. While the tiling is regular in parameter space, it does not account for the curvature of the surface, and thus triangle sizes vary—becoming larger in regions of positive curvature and smaller in regions of negative curvature.

4.2 Quadrature Experiments on the Unit Square

It is standard to verify quadrature convergence by measuring relative error as the mesh is refined (i.e., as the spacing $h \rightarrow 0$). We have performed numerous such experiments and present a representative sample in Section 4.3. Before turning to convergence rates, we first examine specific meshes to illustrate how their structure influences the resulting quadrature weights and errors. This focus is worthwhile because unlike conventional quadrature methods, which require specific node placements (e.g., Gaussian or Newton-Cotes), RBF-based quadrature can accommodate arbitrary node sets. In this setting, mesh spacing h is a useful summary statistics but does not fully determine the node layout or resulting weights.

To demonstrate more precisely, we introduce a qualitative test in which a localized test function smooths the quadrature operator. Specifically, we define a family of steep Gaussian test functions $f_{x_0} : D_1 \rightarrow \mathbb{R}$ by ³

$$f_{x_0}(x) = 2\pi 10^2 \text{ Gauss}(x, x_0; 10) \quad (22)$$

where each function is centered at $x_0 \in D_1$. These Gaussians, defined in eq. (19), using the doubly-periodic distance eq. (18), integrate to the same constant regardless of their center. The mass is sharply localized near x_0 , with rapid decay in all derivatives away from the center. While the periodic distance is not smooth, the resulting test functions are effectively smooth to machine precision. An example is shown in Figure 4.1A.

Figure 4.1B shows the quadrature nodes, colored by their associated weights. We observe that weights along the boundary are consistently smaller. This is partly because boundary nodes appear in fewer stencils, and partly due to mild clustering near the edges—an intentional design to mitigate boundary-related errors such as the Runge phenomenon. Five nodes have negative weights (highlighted with black circles), though each is small in magnitude. The histogram to the right reveals a bimodal distribution: the larger mode is centered near $1/n = 0.0005$, consistent with the average area per node, while the smaller mode corresponds to the boundary-adjacent nodes. This empirical structure reflects both the local stencil geometry and the rule’s enforcement of exactness for constant functions.

We generate approximately $n = 2000$ random and regular nodes (as described in Section 4) and apply the RBF-QF algorithm from Section 3.2 to compute quadrature nodes Ξ and associated weights $\{w_\xi\}_{\xi \in \Xi}$. To assess spatial error, we introduce a relative error as a function of the test function center:

$$E(x_0) = \frac{Qf_{x_0} - Q_n f_{x_0}}{Qf_{x_0}} \quad (23)$$

Large values of $|E(x_0)|$ indicate substantial quadrature error near x_0 , suggesting the local node configuration contributes disproportionately to the total error. This can be interpreted as measuring the relative error in approximating the convolution $(1 * f_{(\cdot)})(x)$ via our quadrature rule.

We use localized Gaussian test functions to visualize how quadrature error varies spatially for different node configurations. In Figure 4.1, we demonstrate this on two node sets in the unit square (See Section 4). Figure 4.1C shows a heatmap of $E(x_0)$, the relative signed quadrature error of our Gaussian test functions f_{x_0} . We again use $n = 2000$ quadrature nodes, the basic function r^3 , a stencil size of $k = 21$, and append third-degree polynomials. The error is relatively small, varies continuously, and is not systematically positive or negative. Most of the error magnitudes are well below the extremal values, highlighting the importance of testing across a variety of test functions.

For this particular mesh, the points are roughly evenly spaced except near the top and bottom boundary where they cluster. Stencils near the boundary are necessarily one sided which can lead to Runge phenomenon [24, 25]. Clustering nodes near these boundaries is one way to combat this and demonstrates the utility of our spatially localized test functions. We observe

³The prefactor of $2\pi 10^2$ has been used in the numerical experiment, but it has no impact on the relative error presented below, and can be safely ignored

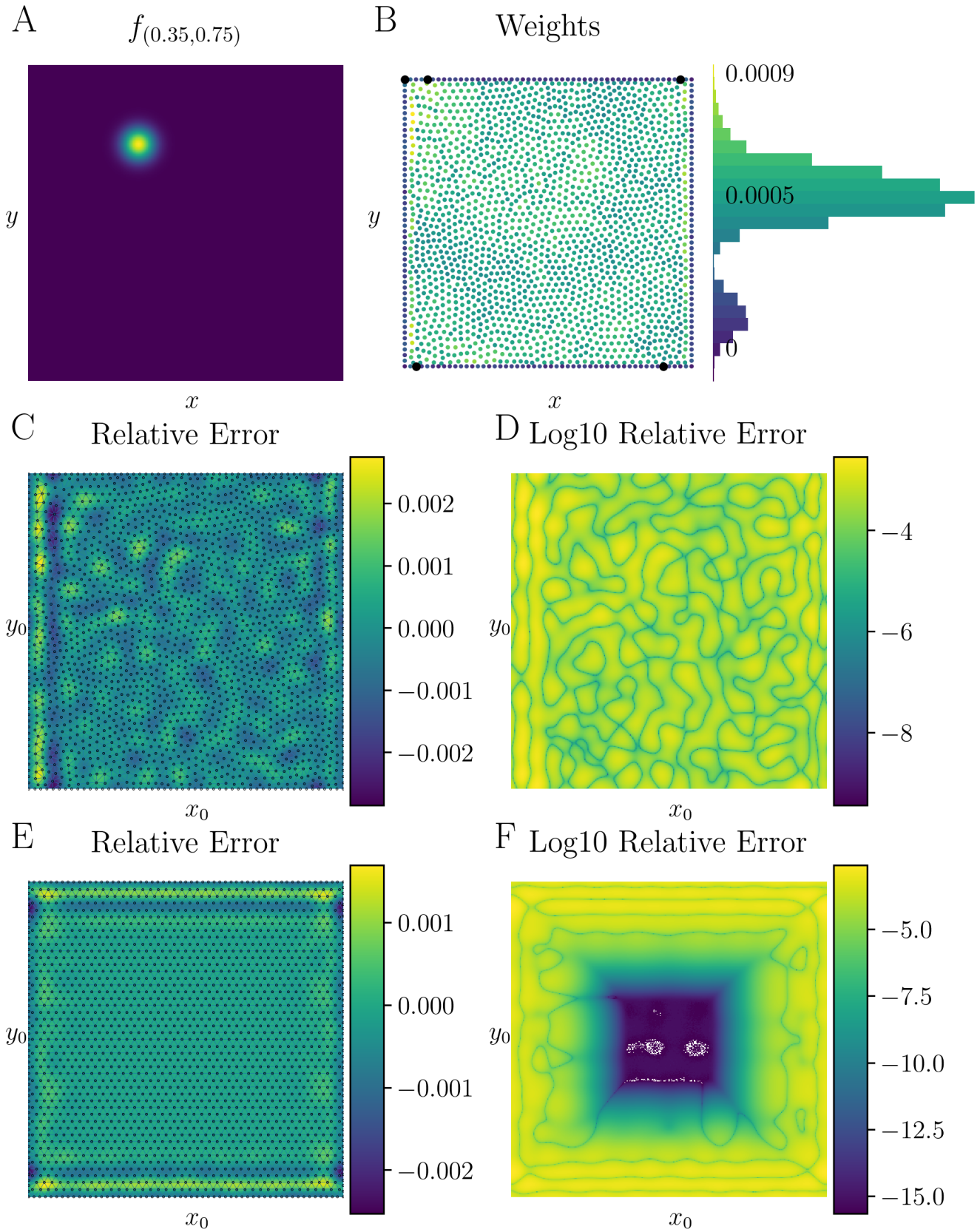


Figure 4.1: **RBF-QF on the Unit Square.** **A.** A single test function as in eq. (22). **B.** Quadrature node locations for $n = 2000$ points, colored by their associated weights. Boundary-adjacent nodes have smaller weights due to asymmetric stencils, and five nodes yield negative weights (black circles). Right: a histogram of weights showing a bimodal distribution—one mode near $1/n = 0.0005$ and a second associated with boundary clustering. **C–D.** Relative error (C) and \log_{10} relative error (D) of the quadrature rule applied to Gaussian test functions f_{x_0} centered throughout the domain. **E–F.** Same as panels C–D, but using a near-regular triangular grid. Interior weights approach $1/n$ and the error approaches machine precision away from the boundary.

that the error is generally higher along the left and right boundaries, where no clustering is applied, and comparatively lower near the top and bottom edges, where node clustering helps control boundary effects.

Any test function can exhibit surprisingly low error due to the random nature of the quadrature nodes. The function $E(\mathbf{x}_0)$ is continuous and oscillatory, and since the quadrature rule integrates constants exactly, the average of E over the domain is zero. The continuity of $E(\mathbf{x}_0)$ follows from the fact that $Q_n f_{\mathbf{x}_0}$ is a continuous function of \mathbf{x}_0 , and $Q f_{\mathbf{x}_0}$ is constant in \mathbf{x}_0 . The average value of E is zero because the quadrature weights are exact for constant functions, a fact that can be verified by a short computation. Thus, there must exist closed curves along which $E(\mathbf{x}_0) = 0$. We visualize this zero-level set by plotting $\log |E(\mathbf{x}_0)|$ in Figure 4.1D. While the overall structure remains similar across different meshes, the precise locations of high and low error regions will vary. This implies that, even for a fixed test function, quadrature error exhibits mesh-dependent spatial variation—even when meshes have similar n and point densities. For this reason, it is common in RBF quadrature studies to generate multiple random node sets for each choice of mesh parameters.

In practice, the presence of small negative weights does not prevent convergence. As noted earlier, Figure 4.1B shows five such weights, each small in magnitude, and their influence appears minimal in Figure 4.1C–D. It is often proposed that a quadrature rule is stable provided

$$\sum_n w_{\xi_n} - \sum_n |w_{\xi_n}| = 0$$

i.e., if all weights are non-negative [29]. High-order Newton–Cotes rules, for instance, fail this criterion and are indeed unstable. However, this notion of stability seems overly restrictive for our purposes. A more lenient condition—one that permits convergence—is that the difference between the total signed and absolute weights remains bounded as $n \rightarrow \infty$ [47, 60]. Indeed, the RBF-QF method has been analyzed under this framework [29], and our experiments confirm that it converges robustly even in the presence of small negative weights.

Lastly, Panels E and F of Figure 4.1 illustrate a case where the quadrature rule achieves spectral accuracy away from the boundary. The test functions and algorithmic parameters remain unchanged, but the nodes are now arranged on a near-regular triangular grid. In this symmetric configuration, the error is extremely small away from the boundary and reaches machine precision near the domain center. The white pixels visible in Panel F result from floating-point coincidence: the analytic integral and quadrature evaluation yield exactly the same double-precision value.

This level of accuracy arises from geometric regularity. When the mesh elements and their associated stencils are rotated translates of each other, the resulting quadrature weights are identical. Coupled with exact integration of constant functions, this symmetry forces all interior weights to equal the average area per node. Importantly, this value is independent of the degree of appended polynomial basis terms, which determine the formal convergence rate. As a result, the quadrature rule achieves arbitrarily high order in the interior—analogue to the spectral accuracy of the trapezoidal rule for periodic functions in one dimension.

4.3 Convergence on the unit square

We evaluate convergence of RBF-QF and neural field simulations on the unit square, using randomly chosen quadrature nodes and triangulations (See Section 4). The test function is $f(x, y) = T_5(2x - 1)T_4(2y - 1)$, a product of Chebyshev polynomials (Figure 4.2 C). Using $\varphi(r) = r^3$ and stencil size $k = 21$, we compute quadrature weights. As shown in Figure 4.2A,C, errors decrease rapidly with increasing appended polynomial degree, often faster than $O(h^{\text{deg}})$. Panel B shows similar convergence for the simulation of the neural field solution, which we now describe.

We next present measured convergence rates for a method of lines simulation of a neural field, using RBF-QF to discretize the weight kernel. The manufactured solution is

$$\begin{aligned} u(t, \mathbf{x}) &= f^{-1} [\text{Gauss}(\mathbf{x}, \mathbf{x}_0(t); \sigma = 11/10) + 1/10], \\ \mathbf{x}_0(t) &= [\cos(t)/5, \sin(t)/5]^T, \end{aligned}$$

which is indeed a solution to eq. (21) on $(t, \mathbf{x}) \in [0, 1/10] \times D_{2\pi}$. Here f is defined in eq. (20), and the weight kernel is $w(\mathbf{x}, \mathbf{y}) = \text{Gauss}(\mathbf{x}, \mathbf{y}; \sigma = 1/40)$ (See eq. (19)). These expressions are used to construct a consistent forcing function. Figure 4.2D shows a snapshot of the resulting traveling bump solution and its circular trajectory, while panel B reports convergence results for different polynomial degrees. In each case, the observed order of accuracy exceeds the expected $O(h^{\text{deg}})$ rate.

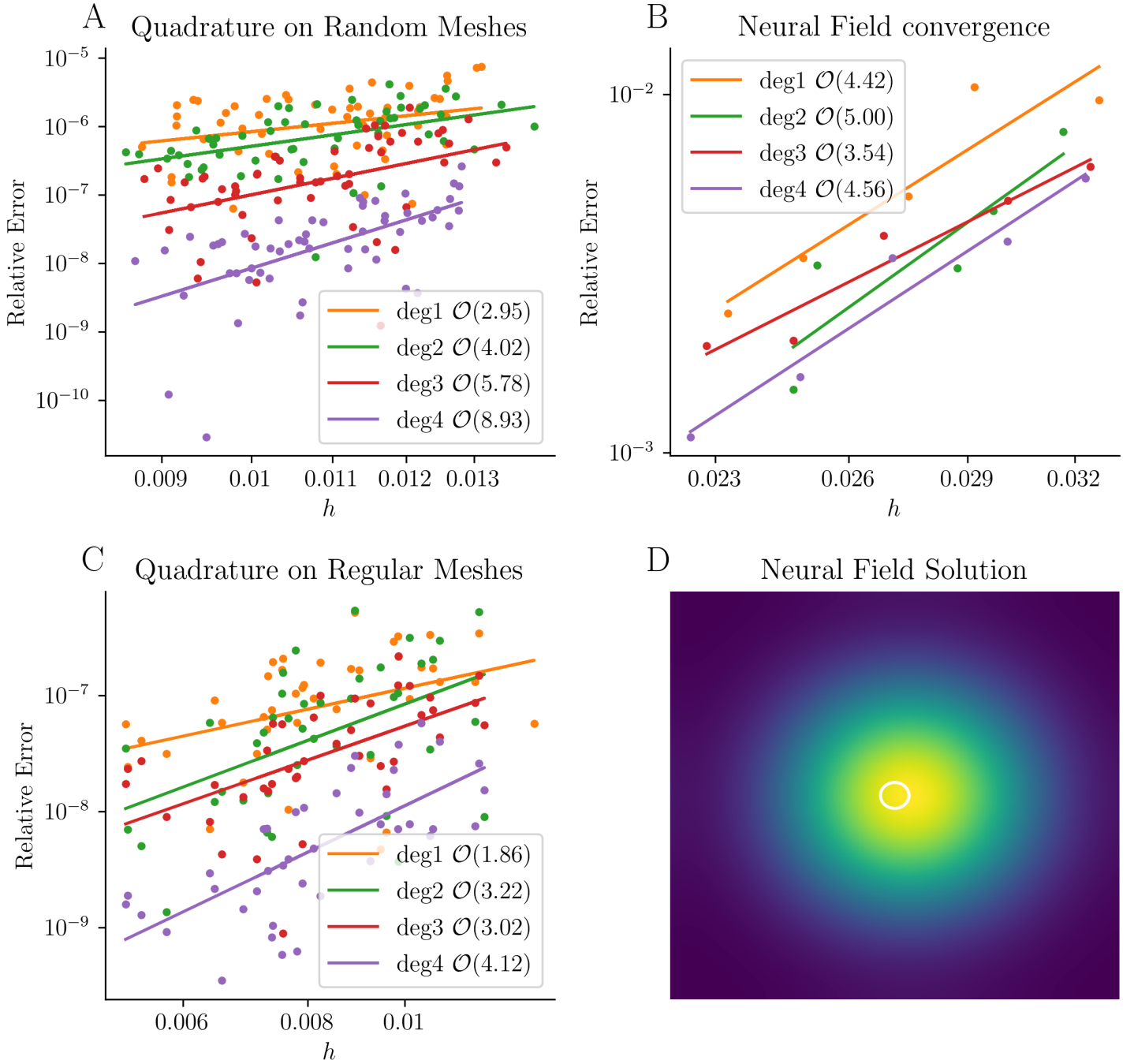


Figure 4.2: **A** Convergence of RBF-QF quadrature for the function $T_5(2x-1)T_4(2y-1)+1$ on the unit square. We use the RBF $\varphi(r) = r^3$, stencil size $k = 21$, and append polynomial terms up to the specified degree (denoted by color). **B** Convergence of a neural field simulation using the same quadrature rules (see main text for details). **C** Same quadrature convergence test as in **A**, but on regular triangular meshes. **D** Neural field solution at times $t = 2n\pi$ ($n \in \mathbb{Z}$), forming a stable bump whose center traces a circular path (shown in white).

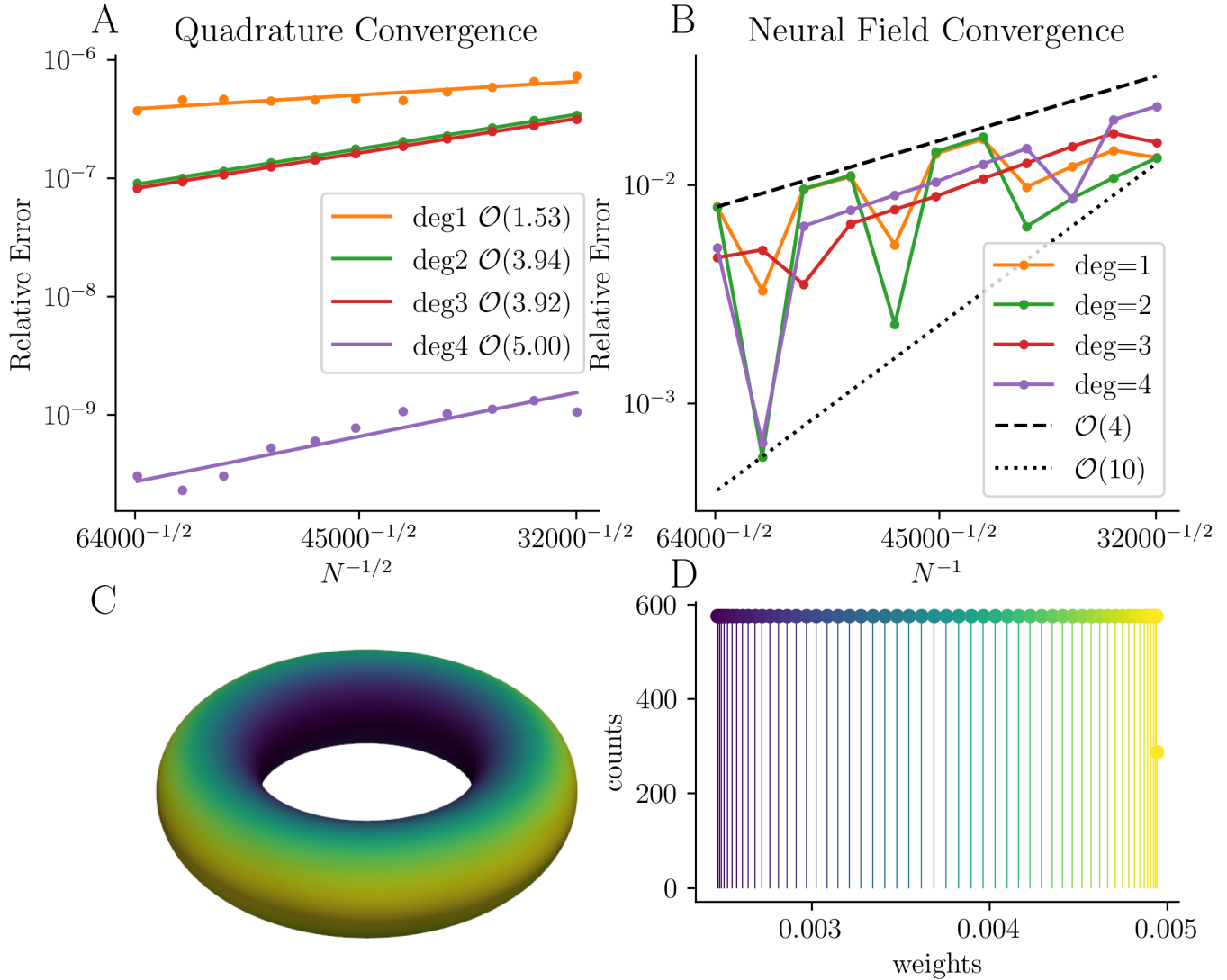


Figure 4.3: **A.** Convergence of surface quadrature on the torus D_T using the test function $f(x, y, z) = \sin(7x) + 1$. In all cases, observed rates exceed the degree of appended polynomials. **B.** Convergence of a neural field simulation using the same surface quadrature rule. **C.** Torus surface colored by the quadrature weights for $k = 12$ and polynomial degree 2. Due to mesh regularity, weights are constant along θ and larger in regions of positive curvature where triangles are bigger. **D** Histogram of the quadrature weights shown in panel C.

4.4 Convergence on a Torus

We next consider convergence results for quadrature and neural field simulations on a torus. For these experiments, we use spiral nodes for the quadrature (See Section 4). While the algorithm does not require such regularity, using spiral nodes simplifies the setup and reduces error variability.

To test the surface RBF-QF algorithm directly, we use the function $f(x, y, z) = \sin(7x) + 1$ on the torus D_T , with $\varphi(r) = r^3$, stencil size $k = 21$, and a polynomial basis appended up to a specified degree. While we lack a direct mesh radius on the surface, the nodes are well spaced, so we use $n^{-1/2} = O(h)$ as a proxy measure of resolution [49, 51]. Figure 4.3A shows that for all polynomial degrees tested, convergence exceeds the expected rate $O(n^{-\text{deg}/2})$.

To test our method of lines neural field simulation on a surface, we construct a manufactured solution analogous to that used in the flat case. Specifically, we let

$$u(t, \mathbf{x}) = f^{-1} [\text{Gauss}(\psi(\mathbf{x}), \mathbf{x}_0; \sigma = 11/10) + 1/10], \quad \mathbf{x}_0 = [\cos(t)/5, \sin(t)/5]^T$$

solve eq. (21) with f as in eq. (20) and weight kernel

$$w(\mathbf{x}, \mathbf{y}) = \text{Gauss}(\psi(\mathbf{x}), \psi(\mathbf{y}); \sigma = 1/40) \frac{1}{(R + r(\mathbf{y}) \cos \theta(\mathbf{y}))}.$$

This mirrors the previous solution but is defined on the surface domain $D_{2\pi}$ (in φ - θ coordinates), with the weight kernel adjusted by the inverse Jacobian of the torus parametrization ($[R + r \cos \theta]^{-1}$). Although the analytical solution is identical, the quadrature weights differ due to the use of surface-specific integration techniques.

Results are shown in Figure 4.3. Panel A shows quadrature convergence on the torus using the test function $f(x, y, z) = \sin(7x) + 1$ with relative error decreasing as $n^{-1/2}$ and higher decay rates for higher-degree appended polynomials. Panel B reports convergence for the manufactured neural field solution, again showing high-order accuracy. Panel C visualizes the quadrature weights across the torus surface for $n = 32000$, while D presents a histogram of these weights. Weights are constant along lines of constant θ due to the symmetry of the node placement; their distribution reflects both curvature effects and histogram binning.

5 Showcase of neural field dynamics on curved geometries

Thus far, we have described and tested a numerical method for solving neural field equations on smooth, closed manifolds. In this section, we demonstrate its utility with simulations that reveal rich spatiotemporal dynamics on curved geometries. Each example extends classical results from planar or one-dimensional settings to non-Euclidean domains, identifying impacts and considerations of curvature on solution dynamics, opening new avenues for mathematical and scientific investigation. All computations use the same geodesic distance approximation, described in the **Code Availability** section.

5.1 Labyrinthine patterns on a deformed sphere

Previously, Coombes et al [20] investigated a neural field model in two spatial dimensions that exhibits *labyrinthine patterns* under appropriate initial condition. These patterns emerge when a lateral inhibitory weight kernel is used with an unstable, near symmetric bump initial activity profile. Owing to the D_4 symmetry of the dominant instability, four arms of a cross extend outward from the bump and begin to branch, producing a single connected region of high neural activity, forming a complex labyrinth of thin, repeatedly branching corridors.

We perform a similar numerical experiment on a family of deformed spheres, demonstrating that surface curvature has a significant effect on the qualitative properties of the resulting labyrinthine patterns. Unlike the original experiment by Coombes et al. [20], which employed a discontinuous Heaviside firing-rate function and a non-smooth weight kernel, we use smooth, qualitatively similar functions that still give rise to complex spatiotemporal activity. Specifically, we define the weight

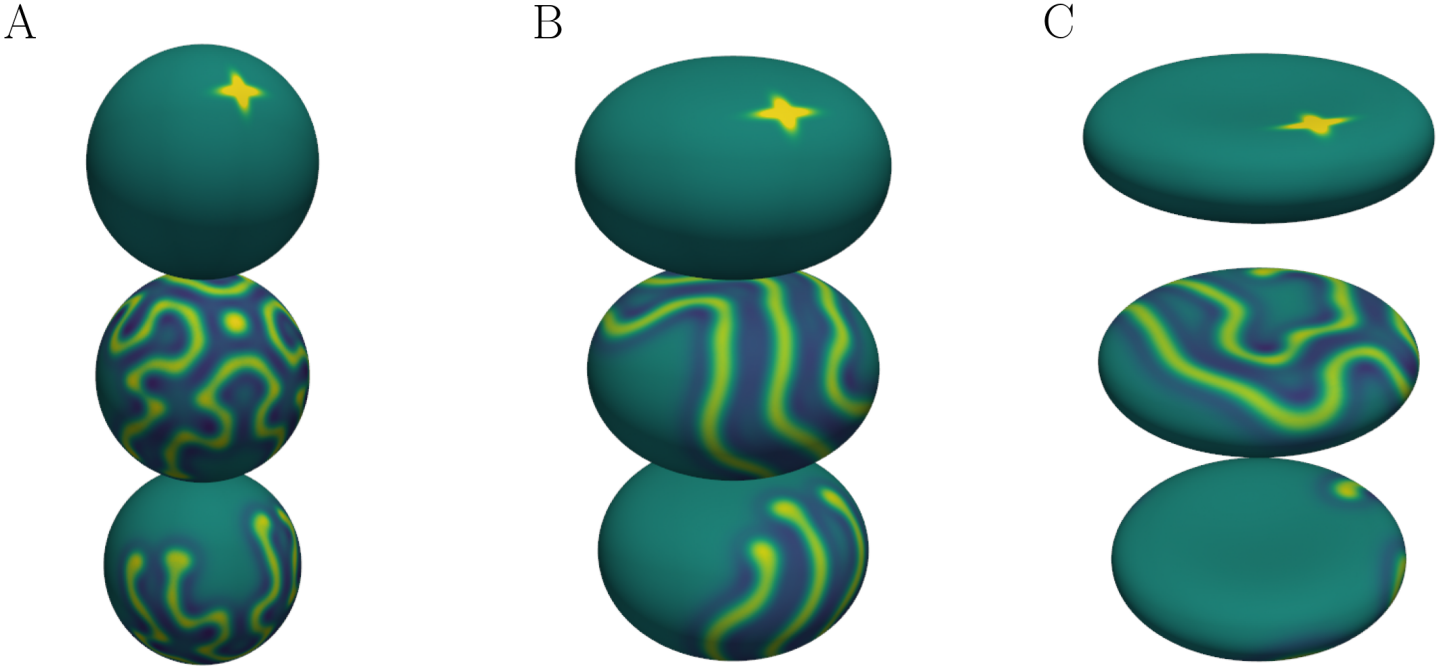


Figure 5.1: **Effect of Surface Deformation on Labyrinthine Patterns.** Labyrinthine patterns on a deformed spherical surface D_γ , with increasing deformation parameter from left to right: **A.** $\gamma = 0$ (perfect sphere), **B.** $\gamma = 0.4$ (moderate deformation), **C.** $\gamma = 0.8$ (flattened, blood-cell-like shape). The top row shows the initial unstable, cross-shaped activity pattern. The middle and bottom rows show the resulting spatiotemporal patterns from two viewpoints: with the north and south poles facing the viewer, respectively. Yellow indicates high neural activity ($u > 0$), green denotes baseline activity ($u \approx 0$), and dark green/blue indicates suppressed activity ($u < 0$). Surface curvature has a profound effect on the form and complexity of the resulting patterns. Click image to view full animation (Movie S1A, Movie S1B, Movie S1C).

kernel and firing-rate function as

$$w(\mathbf{x}, \mathbf{y}) = A_e \text{Gauss}(\mathbf{x}, \mathbf{y}, \sigma_e) - A_i \text{Gauss}(\mathbf{x}, \mathbf{y}, \sigma_i), \quad (24)$$

$$f(u) = \begin{cases} 0, & u < 0.06, \\ p(u), & 0.06 \leq u < 0.54, \\ 1, & u \geq 0.54, \end{cases} \quad (25)$$

where $A_e = 5$, $A_i = 5$, $\sigma_e = 0.05$, $\sigma_i = 0.1$. Although $A_e = A_i$, the kernel satisfies $w(\mathbf{x}, \mathbf{x}) > 0$ since the Gaussian is normalized – its peak is higher for smaller σ – producing the desired lateral inhibitory property. The function $p(u)$ is a 9th-order polynomial chosen to ensure that f is four times continuously differentiable, yielding a smooth spline approximation to the Heaviside function $H(u - 0.3)$, remaining constant outside a narrow transition interval centered at the threshold.

The underlying surface D_γ is a one-parameter family of deformed spheres, with deformation governed by $\gamma \in [0, 1)$. When $\gamma = 0$, the surface is a standard sphere; as γ increases, the geometry is increasingly compressed along the vertical axis, reducing the pole-to-pole Euclidean distance to $2(1 - \gamma)$. The surface is implicitly defined by

$$1 = x^2 + y^2 + z^2 \left(1 - \frac{\gamma}{1 + (x^2 + y^2)/2.89} \right)^{-1},$$

and is visualized in Figure 5.1 for $\gamma = 0, 0.4, 0.8$.

We initialize the activity $u(0, \mathbf{x})$ on the undeformed sphere using the function

$$u(0, \mathbf{x}) = 5 \cdot \exp \left(-10 \left[\left(\cos \left(4 \arctan \left(\frac{y}{x} \right) \right) + 3 \right) \sqrt{x^2 + y^2} \right]^2 \right) H(z),$$

which defines a symmetric, cross-shaped pattern localized in the northern hemisphere. To orient this pattern appropriately, we apply a rigid rotation that maps the north pole $[0, 0, 1]$ to the point $[0.5, 0.3, \sqrt{0.5^2 + 0.3^2}]$, aligning the initial condition with the desired surface region before the deformation is applied.

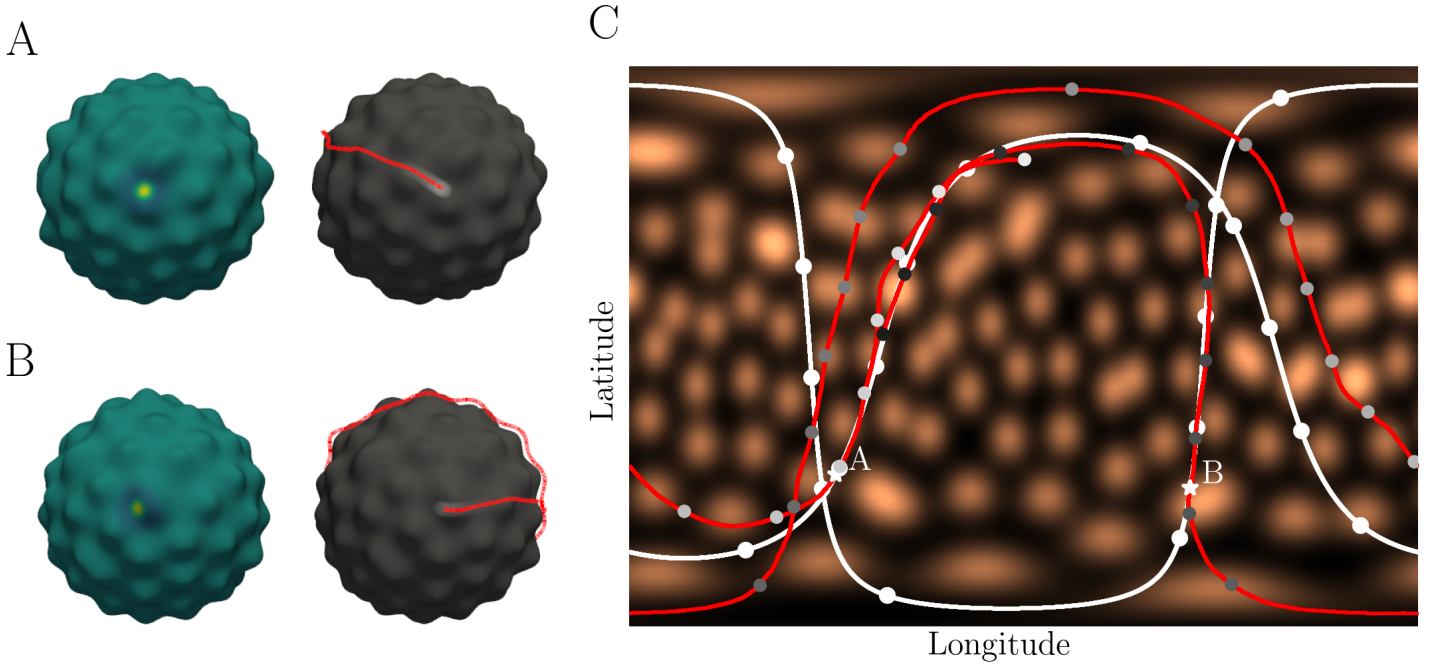


Figure 5.2: **Traveling spot steered by bumps in curvature.** **A–B:** Snapshots from a simulation of a traveling spot on a bumpy sphere. Each snapshot shows two views: the left sphere is colored by the activity variable, and the right is shaded by the synaptic efficacy. The trajectory of the spot up to that point is shown as a red curve hovering above the surface. **C:** Projection of the bumpy surface into spherical coordinates, with longitude on the horizontal axis, latitude on the vertical axis, and surface elevation encoded by heatmap. Traveling spot trajectory (red) sometimes hugs but also deviates from great-circle tangents (white) aligned with spot position in panels **A** and **B**, showing how bumps deflect motion. Click image to view full animation (Movie S2).

We then simulate the neural field on each deformed surface using the kernel basis function $\varphi(r) = r^3$, a stencil size of $k = 32$, and append third-degree polynomials for accurate quadrature. Time integration is performed using the Adams–Bashforth 5 method with a fixed time step of $\Delta t = 10^{-2}$. The resulting dynamics, corresponding to various values of the surface deformation parameter $\gamma = 0, 0.4, 0.8$, are shown in Figure 5.1. The top row depicts the initial condition, rendered from a viewpoint where the *north pole* is visible. The middle row shows the activity at time $t = 200$ from the same viewpoint, while the bottom row presents the state at $t = 200$ with the surface inverted through the x - y plane to reveal the *south pole*.

Labyrinthine corridors remain connected but their wandering termini tend to veer away from regions of high curvature, illustrate how surface geometry profoundly influences neural field dynamics. This is akin to the pinning of propagating waves [9, 19] or attraction/repulsion of localized activity [34] observed by introducing inhomogeneities into the weight kernel of neural fields on flat domains.

5.2 Traveling spot steered by surface bumps

Our next example demonstrates how surface curvature influences the trajectory of traveling spot solutions in a neural field model with synaptic depression [13, 55]. The model consists of two coupled equations: one for the neural activity u , and one for the synaptic efficacy q , ranging from 0 (depleted) to 1 (fully available). The dynamics are given by

$$\partial_t u = -u + \int_D w(_, \mathbf{y}) q(_, \mathbf{y}) f[u(_, \mathbf{y})] d\mathbf{y}, \quad \tau \partial_t q = 1 - q - \beta q f[u]. \quad (26)$$

We use the laterally inhibitory weight kernel eq. (24) with $A_e = 5$, $A_i = 7$, $\sigma_e = 0.05$, $\sigma_i = 0.1$. Such weights often produce *spot* solutions (localized circular active regions, also called pulses or bumps) in planar neural fields without adaptation ($\beta = 0$).

Incorporating synaptic depression ($\beta > 0$), as with other forms of adaptation [42], causes spots to travel. Introducing depression ($q < 1$) on one side of the spot, effective lateral inhibition is asymmetric and activity will increase on the side of the spot farthest from the depressed region [13, 55]. The spot then propagates, leaving a trail of synaptic depression in its wake.

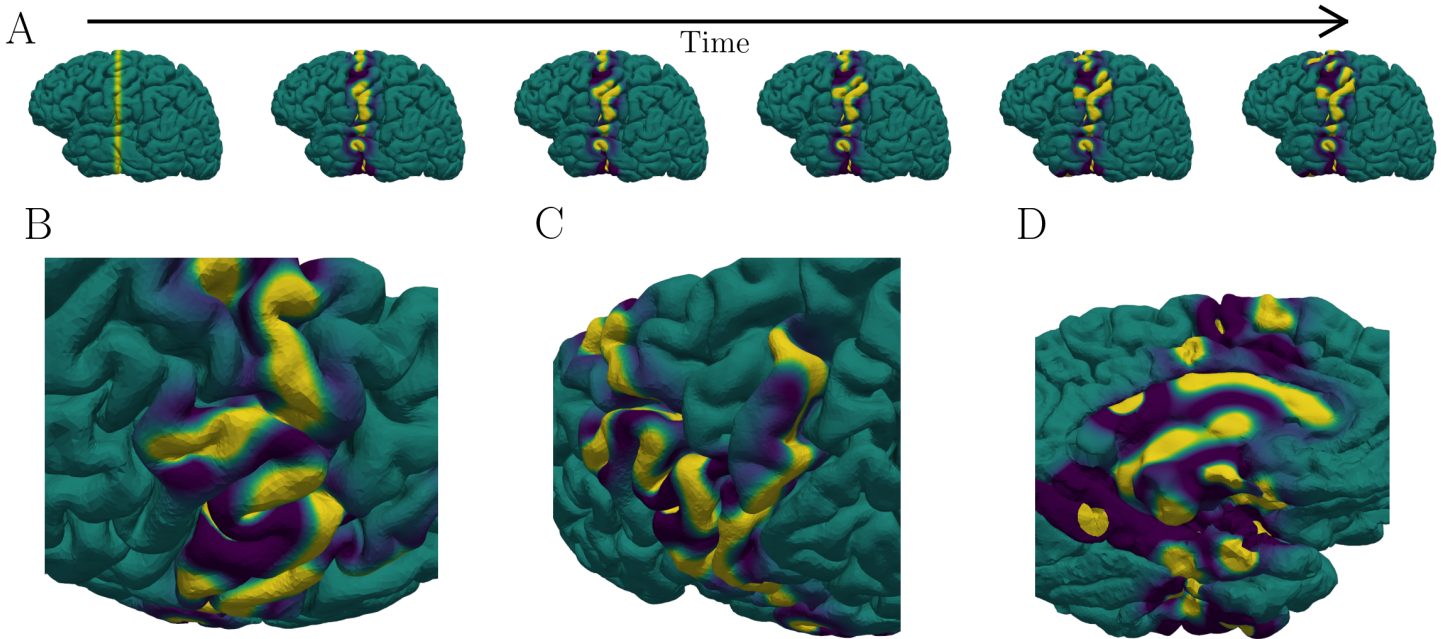


Figure 5.3: **Labyrinthine dynamics on a cortex.** Here we show a simulation on the left hemisphere of a realistic human cortex using a laterally inhibitory weight kernel that favors the formation of labyrinthine patterns. **A:** Snapshots at evenly spaced early time points show the initial stripe of activity breaking into multiple labyrinth-like corridors that begin to grow and evolve. **B–D:** Final-time snapshots from different viewing angles highlight distinct cortical regions: **B.** frontal lobe, **C.** parietal lobe, and **D.** limbic cortex/medial surface. Click image to view full animation (Movie S3).

We probe how surface curvature affects trajectories of such traveling spots by considering a surface that we refer to as a *bumpy sphere* (Figure 5.2), defined by the equation:

$$1 + \sum_{\mathbf{x}_i} \text{Gauss}'(\mathbf{x}, \mathbf{x}_i, 1/10)/10 = x^2 + y^2 + z^2$$

where $\{\mathbf{x}_i\}_{i=1}^{100}$ are a set of 100 *bump centers* (randomly chosen, though roughly evenly spaced) on the unit sphere (See remarks in **Code Availability** section).

Figure 5.2A and B each show two snapshots from the same simulation, each depicting two views of the bumpy sphere. The left view is colored by the activity variable, while the right shows synaptic efficacy in grayscale. Both are rotated to center the spot in view, and the grayscale surface includes a red curve tracing the trajectory of the spot up to that time. Figure 5.2C presents the surface in spherical coordinates, with latitude and longitude along the vertical and horizontal axis, and color representing radial elevation. The red curve shows the full trajectory of the traveling spot. If the surface were perfectly spherical, the spot would follow a straight path along a great circle, akin to what was found on the planar case [13]. Instead, we observe consistent deviations in the trajectory that arise from geometric inhomogeneities. Two white curves show tangent great circles at times shown in panels A and B, illustrating how the trajectory is deflected by geometric inhomogeneities. This reinforces the point that surface irregularities creates a similar potential surface which shape the dynamics of evolving spatiotemporal solutions, akin to those created in neural fields on flat domains with weight inhomogeneities [36,46].

5.3 Labyrinthine patterns on a human cortex

Finally, we build a simulation showcasing the evolution of a neural field on a cortical surface extracted from human data (Figure 5.3). See **Code Availability** for a link to the repository containing this mesh, representing the left hemisphere of a human cortex. It was generated using MNE-Python, which integrates FreeSurfer’s anatomical reconstruction pipeline to segment T1-weighted MRI scans and extract detailed cortical surfaces. The resulting triangulated mesh captures the geometry of the pial surface, including sulci and gyri, enabling anatomically realistic neural field simulations. We use the same laterally inhibitory weight function defined in eq. (24) with $A_e = A_i = 5$, $\sigma_e = 3$, $\sigma_i = 6$, along with the geodesic distance metric and parameters from Section 5.1. The initial condition consists of a band of activity, which rapidly fragments into localized

regions of varying size shaped by the surface curvature. The resulting dynamics include both stationary spots and labyrinthine corridors that tend to follow gyri and sulci—regions aligned with locally minimal curvature.

The mesh used here is visually compelling and anatomically detailed, though originally intended for visualization rather than numerical simulation. It exhibits some geometric irregularities – including a small duplicated region, uneven node density, and inconsistencies in surface normals. This leads to rapidly oscillating quadrature weights, including some large negative values. Nonetheless, the resulting dynamics reveal rich qualitative structure that underscores the potential of this framework and motivates further refinement and study.

Although a rigorous analytical treatment of these effects on curved surfaces remains an open question, these results highlight the potential for geometry to shape the dynamics of cortical activity. Our framework provides a powerful computational tool for probing such curvature-driven effects in structured neural field models.

6 Conclusion

We have presented a high-order, mesh-flexible solver for neural fields on smooth, closed surfaces, using RBF-based interpolation and quadrature. This method is numerically stable, accurate, and only requires a triangulated surface mesh and approximate vertex normals. Unlike spectral methods, which typically require structured domains, our approach—like finite element methods—can be applied to arbitrary geometries. However, it offers additional flexibility in simulating neural fields on domains with complex curvature without requiring a mesh. The sparse quadrature matrices produced by this scheme still have quadratic computational complexity in the number of nodes due to the pairwise interactions involved. This scaling presents a practical bottleneck, making it especially important to achieve high accuracy with fewer nodes—hence the motivation for high-order methods. This tradeoff is crucial when modeling cortex-scale dynamics or pursuing inverse problems where kernel learning is computationally intensive.

Neural field simulation can thus be performed on deformed/bumpy spheres and realistic human cortical surfaces, where geometry significantly shapes activity patterns. Our results mirror phenomena observed in planar neural fields with inhomogeneous coupling—such as wave pinning and curvature-guided propagation—and show that similar principles extend to curved domains.

We also note that it is common to couple neural field equations with differential equations, or to otherwise include spatial differential operators, commonly diffusion [5, 35]. There are a variety of radial basis function finite difference techniques that approximate operators such as surface advection or surface diffusion that pair nicely with this method [27, 39, 43, 45, 54, 56]. Specifically, the computation of quadrature weights and the computation of finite-difference weights requires solving linear systems with the same matrix, giving opportunity for savings (though the order of accuracy will depend on the order of the differential operator). More importantly, these methods will be high-order and geometrically flexible.

Our results illustrate the type of experiments this method enables and suggest many directions for exploration. In Figure 5.1, the gyrus-like ridge appears to steer the wandering labyrinth along low-curvature paths, confining it to one side until repulsion from other corridors forces a transition. Similar behavior is seen on actual gyri in Figure 5.3. It would be interesting to study how the shape and excitatory–inhibitory balance of the kernel contribute to curvature-guided dynamics, how surface geometry steers traveling spots, and whether a critical angle of incidence maximizes deflection.

The bumpy sphere experiment in Figure 5.2 shows that curvature deflects traveling spot trajectories. Its effects on speed or stability remain unclear, though prior work suggests curvature can pin or disrupt waves [9, 19]. In multi-spot simulations, we observed curvature-modulated crowding and spot death [34, 46]. Future work could reduce spot dynamics to effective equations or study curvature-driven pinning and annihilation [11, 41]. These simulations also invite asymptotic approaches, such as interface methods in the high-gain limit [20], perturbation theory for bump drift [11, 34], or even weakly nonlinear analysis for patterns near bifurcations [61].

Our method leverages only surface geometry and admits arbitrary kernels, providing a promising platform for pairing with experimental data to learn connectivity kernels directly. This opens doors to data-driven modeling, model inversion, and further theoretical studies of how cortical geometry sculpts large-scale dynamics.

Code Availability

Repository addresses containing code developed for implementing quadrature and time-stepping are here: quadrature weight generation: <https://github.com/shawsa/neural-fields-rbf>; node generation: https://github.com/shawsa/min_energy_points; numerical time-integration: <https://github.com/shawsa/odeiter>. For curved domains, the first order approximation to the geodesic distance via the Fast Marching Algorithm [53] can be found in the MeshLib library: <https://meshlib.io/>. Precise centers of bumps on the bumpy sphere are given in <https://github.com/shawsa/neural-fields-rbf>. The realistic cortical mesh was adapted from the MNE python library: <https://mne.tools/stable/index.html>.

References

- [1] S. AMARI, *Dynamics of pattern formation in lateral-inhibition type neural fields*, Biological cybernetics, 27 (1977), pp. 77–87.
- [2] K. E. ATKINSON, *The Numerical Solution of Integral Equations of the Second Kind*, Cambridge Monographs on Applied and Computational Mathematics, Cambridge University Press, 1997.
- [3] K. E. ATKINSON AND W. HAN, *Theoretical numerical analysis*, vol. 39, Springer, 2005.
- [4] D. AVITABILE, *Projection Methods for Neural Field Equations*, SIAM Journal on Numerical Analysis, 61 (2023), pp. 562–591.
- [5] E. BASPINAR, D. AVITABILE, M. DESROCHES, AND M. MANTEGAZZA, *A neural field model for ignition and propagation of cortical spreading depression*. working paper or preprint, Feb. 2023, <https://hal.science/hal-04008117>.
- [6] V. BAYONA, N. FLYER, AND B. FORNBERG, *On the role of polynomials in rbf-fd approximations: Iii. behavior near domain boundaries*, Journal of Computational Physics, 380 (2019), pp. 378–399.
- [7] V. BAYONA, N. FLYER, B. FORNBERG, AND G. A. BARNETT, *On the role of polynomials in rbf-fd approximations: Ii. numerical solution of elliptic pdes*, Journal of Computational Physics, 332 (2017), pp. 257–273.
- [8] M. BREAKSPEAR, *Dynamic models of large-scale brain activity*, Nature neuroscience, 20 (2017), pp. 340–352.
- [9] P. C. BRESSLOFF, *Traveling fronts and wave propagation failure in an inhomogeneous neural network*, Physica D: Nonlinear Phenomena, 155 (2001), pp. 83–100.
- [10] P. C. BRESSLOFF, *Spatiotemporal dynamics of continuum neural fields*, Journal of Physics A: Mathematical and Theoretical, 45 (2011), p. 033001.
- [11] P. C. BRESSLOFF, *Stochastic neural field theory of wandering bumps on a sphere*, Physica D: Nonlinear Phenomena, 399 (2019), pp. 138–152.
- [12] P. C. BRESSLOFF AND J. D. COWAN, *A spherical model for orientation and spatial-frequency tuning in a cortical hypercolumn*, Philosophical Transactions of the Royal Society of London. Series B: Biological Sciences, 358 (2003), pp. 1643–1667.
- [13] P. C. BRESSLOFF AND Z. P. KILPATRICK, *Two-dimensional bumps in piecewise smooth neural fields with synaptic depression*, SIAM Journal on Applied Mathematics, 71 (2011), pp. 379–408.
- [14] M. BUHMANN AND N. DYN, *Spectral convergence of multiquadric interpolation*, Proceedings of the Edinburgh Mathematical Society, 36 (1993), pp. 319–333.
- [15] M. D. BUHMANN, *Radial basis functions*, Acta Numerica, 9 (2000), pp. 1–38. Publisher: Cambridge University Press.
- [16] T. CECIL, J. QIAN, AND S. OSHER, *Numerical methods for high dimensional hamilton-jacobi equations using radial basis functions*, Journal of Computational Physics, 196 (2004), pp. 327–347.

- [17] S. COOMBES, *Large-scale neural dynamics: simple and complex*, NeuroImage, 52 (2010), pp. 731–739.
- [18] S. COOMBES, P. BEIM GRABEN, R. POTTHAST, AND J. WRIGHT, *Neural fields: theory and applications*, Springer, 2014.
- [19] S. COOMBES AND C. LAING, *Pulsating fronts in periodically modulated neural field models*, Physical Review E—Statistical, Nonlinear, and Soft Matter Physics, 83 (2011), p. 011912.
- [20] S. COOMBES, H. SCHMIDT, AND I. BOJAK, *Interface dynamics in planar neural field models*, The Journal of Mathematical Neuroscience, 2 (2012), pp. 1–27.
- [21] S. COOMBES, N. A. VENKOV, L. SHIAU, I. BOJAK, D. T. LILEY, AND C. R. LAING, *Modeling electrocortical activity through improved local approximations of integral neural field equations*, Physical Review E—Statistical, Nonlinear, and Soft Matter Physics, 76 (2007), p. 051901.
- [22] P. C. CURTIS, *n-parameter families and best approximation.*, Pacific J. Math., 9 (1959), pp. 1013–1027.
- [23] G. F. FASSHAUER, *Meshfree Approximation Methods with MATLAB*, World Scientific Publishing Co., Inc., River Edge, NJ, USA, 2007.
- [24] N. FLYER, B. FORNBERG, V. BAYONA, AND G. A. BARNETT, *On the role of polynomials in rbf-fd approximations: I. interpolation and accuracy*, Journal of Computational Physics, 321 (2016), pp. 21–38.
- [25] B. FORNBERG AND J. ZUEV, *The runge phenomenon and spatially variable shape parameters in rbf interpolation*, Computers & Mathematics with Applications, 54 (2007), pp. 379–398.
- [26] S. FORTUNE, *Voronoi diagrams and delaunay triangulations*, in Handbook of discrete and computational geometry, Chapman and Hall/CRC, 2017, pp. 705–721.
- [27] E. J. FUSELIER AND G. B. WRIGHT, *A high-order kernel method for diffusion and reaction-diffusion equations on surfaces*, Journal of Scientific Computing, 56 (2013), pp. 535–565.
- [28] P. GAO AND S. GANGULI, *On simplicity and complexity in the brave new world of large-scale neuroscience*, Current opinion in neurobiology, 32 (2015), pp. 148–155.
- [29] J. GLAUBITZ AND J. A. REEGER, *Towards stability results for global radial basis function based quadrature formulas*, BIT Numerical Mathematics, 63 (2023), p. 6.
- [30] R. L. HARDY, *Multiquadric equations of topography and other irregular surfaces*, Journal of Geophysical Research (1896-1977), 76 (1971), pp. 1905–1915.
- [31] X. HUANG, W. XU, J. LIANG, K. TAKAGAKI, X. GAO, AND J.-Y. WU, *Spiral wave dynamics in neocortex*, Neuron, 68 (2010), pp. 978–990.
- [32] M. J. JOHNSON, *On The Error In Surface Spline Interpolation Of A Compactly Supported Function*. 1998.
- [33] E. KANSA, *Multiquadrics—a scattered data approximation scheme with applications to computational fluid-dynamics—ii solutions to parabolic, hyperbolic and elliptic partial differential equations*, Computers & Mathematics with Applications, 19 (1990), pp. 147 – 161.
- [34] Z. P. KILPATRICK AND B. ERMENTROUT, *Wandering bumps in stochastic neural fields*, SIAM Journal on Applied Dynamical Systems, 12 (2013), pp. 61–94.
- [35] F. KNEER, E. SCHÖLL, AND M. A. DAHLEM, *Nucleation of reaction-diffusion waves on curved surfaces*, New Journal of Physics, 16 (2014), p. 053010.
- [36] C. KUEHN AND J. M. TÖLLE, *A gradient flow formulation for the stochastic amari neural field model*, Journal of mathematical biology, 79 (2019), pp. 1227–1252.

- [37] C. R. LAING AND W. C. TROY, *Pde methods for nonlocal models*, SIAM Journal on Applied Dynamical Systems, 2 (2003), pp. 487–516.
- [38] S.-H. LEE, R. BLAKE, AND D. J. HEEGER, *Traveling waves of activity in primary visual cortex during binocular rivalry*, Nature neuroscience, 8 (2005), pp. 22–23.
- [39] E. LEHTO, V. SHANKAR, AND G. B. WRIGHT, *A radial basis function (rbf) compact finite difference (fd) scheme for reaction-diffusion equations on surfaces*, SIAM Journal on Scientific Computing, 39 (2017), pp. A2129–A2151.
- [40] J. C. MAIRHUBER, *On haar’s theorem concerning chebychev approximation problems having unique solutions*, Proceedings of the American Mathematical Society, 7 (1956), pp. 609–615.
- [41] R. MARTIN, D. J. CHAPPELL, N. CHUZHANOVA, AND J. J. CROFTS, *A numerical simulation of neural fields on curved geometries*, Journal of computational neuroscience, 45 (2018), pp. 133–145.
- [42] M. R. OWEN, C. R. LAING, AND S. COOMBES, *Bumps and rings in a two-dimensional neural field: splitting and rotational instabilities*, New Journal of Physics, 9 (2007), p. 378.
- [43] A. PETRAS, L. LING, AND S. J. RUUTH, *An rbf-fd closest point method for solving pdes on surfaces*, Journal of Computational Physics, 370 (2018), pp. 43–57.
- [44] D. J. PINTO AND G. B. ERMENTROUT, *Spatially structured activity in synaptically coupled neuronal networks: I. traveling fronts and pulses*, SIAM journal on Applied Mathematics, 62 (2001), pp. 206–225.
- [45] C. PIRET, *The orthogonal gradients method: A radial basis functions method for solving partial differential equations on arbitrary surfaces*, Journal of Computational Physics, 231 (2012), pp. 4662–4675.
- [46] D. POLL AND Z. P. KILPATRICK, *Stochastic motion of bumps in planar neural fields*, SIAM Journal on Applied Mathematics, 75 (2015), pp. 1553–1577.
- [47] G. PÓLYA, *Über die konvergenz von quadraturverfahren*, Mathematische Zeitschrift, 37 (1933), pp. 134, 264–286.
- [48] R. POTTHAST AND P. BEIM GRABEN, *Existence and properties of solutions for neural field equations*, Mathematical Methods in the Applied Sciences, 33 (2010), pp. 935–949.
- [49] J. REEGER, B. FORNBERG, AND M. WATTS, *Numerical quadrature over smooth, closed surfaces*, Proceedings of the Royal Society A: Mathematical, Physical and Engineering Sciences, 472 (2016), p. 20160401.
- [50] J. A. REEGER AND B. FORNBERG, *Numerical quadrature over the surface of a sphere*, Studies in Applied Mathematics, 137 (2016), pp. 174–188.
- [51] J. A. REEGER AND B. FORNBERG, *Numerical quadrature over smooth surfaces with boundaries*, Journal of Computational Physics, 355 (2018), pp. 176–190.
- [52] P. A. ROBINSON, C. J. RENNIE, AND J. J. WRIGHT, *Propagation and stability of waves of electrical activity in the cerebral cortex*, Physical Review E, 56 (1997), p. 826.
- [53] J. A. SETHIAN, *A fast marching level set method for monotonically advancing fronts.*, proceedings of the National Academy of Sciences, 93 (1996), pp. 1591–1595.
- [54] V. SHANKAR, G. B. WRIGHT, R. M. KIRBY, AND A. L. FOGELSON, *A radial basis function (rbf)-finite difference (fd) method for diffusion and reaction–diffusion equations on surfaces*, Journal of scientific computing, 63 (2015), pp. 745–768.
- [55] S. SHAW AND Z. P. KILPATRICK, *Representing stimulus motion with waves in adaptive neural fields*, Journal of computational neuroscience, 52 (2024), pp. 145–164.
- [56] S. B. SHAW, *Radial basis function finite difference approximations of the laplace-beltrami operator*, master’s thesis, Boise State University, 2019.

- [57] S. SHIPP, *Structure and function of the cerebral cortex*, Current Biology, 17 (2007), pp. R443–R449.
- [58] C. SHU, H. DING, AND K. YEO, *Local radial basis function-based differential quadrature method and its application to solve two-dimensional incompressible navier–stokes equations*, Computer methods in applied mechanics and engineering, 192 (2003), pp. 941–954.
- [59] A. I. TOLSTYKH AND D. SHIROBOKOV, *On using radial basis functions in a “finite difference mode” with applications to elasticity problems*, Computational Mechanics, 33 (2003), pp. 68–79.
- [60] L. N. TREFETHEN, *Exactness of quadrature formulas*, Siam Review, 64 (2022), pp. 132–150.
- [61] N. A. VENKOV, S. COOMBES, AND P. C. MATTHEWS, *Dynamic instabilities in scalar neural field equations with space-dependent delays*, Physica D: Nonlinear Phenomena, 232 (2007), pp. 1–15.
- [62] S. VISSER, R. NICKS, O. FAUGERAS, AND S. COOMBES, *Standing and travelling waves in a spherical brain model: the nunez model revisited*, Physica D: Nonlinear Phenomena, 349 (2017), pp. 27–45.
- [63] H. WENDLAND, *Scattered Data Approximation*, Cambridge Monographs on Applied and Computational Mathematics, Cambridge University Press, 2004.
- [64] H. R. WILSON AND J. D. COWAN, *A mathematical theory of the functional dynamics of cortical and thalamic nervous tissue*, Kybernetik, 13 (1973), pp. 55–80.
- [65] H. R. WILSON AND J. D. COWAN, *A mathematical theory of the functional dynamics of cortical and thalamic nervous tissue*, Kybernetik, 13 (1973), pp. 55–80.
- [66] G. B. WRIGHT, *Radial basis function interpolation: numerical and analytical developments*, University of Colorado at Boulder, 2003.
- [67] J. YOON, *Spectral approximation orders of radial basis function interpolation on the sobolev space*, SIAM journal on mathematical analysis, 33 (2001), pp. 946–958.